Synthesis, Structure and Spectroscopic Investigations of Luminescent Heterobimetallic Gold(I)-Rhodium(I) Species

by

Jillian Lee Dempsey

Submitted to the Department of Chemistry
as supplement to the requirements for the degree of

Bachelor of Science in Chemistry

at the

MASSACHUSETTS INSTITUTE OF TECHNOLOGY

June 2005

Author.....
Department of Chemistry
April 2005

Certified by.....
Daniel G. Nocera
Thesis Supervisor

Accepted by.....
Rick L. Danheiser
Chairman, Department Committee on Undergraduate Students

Synthesis, Structure and Spectroscopic Investigations of Luminescent Heterobimetallic Gold(I)-Rhodium(I) Species

by

Jillian Lee Dempsey

Submitted to the Department of Chemistry
as supplement to the requirements for the degree of

Bachelor of Science in Chemistry

Abstract

A novel, three-coordinate gold(I) dimer, $Au_2(tfepm)_3Cl_2$ (**1a**, **1b**), was synthesized and structurally characterized. Four gold(I)-rhodium(I) heterobimetallic complexes, $Au^IRh^I(^tBuNC)_2(\mu\text{-dppm})_2Cl_2$ (**2**), $Au^IRh^I(^tBuNC)_2(\mu\text{-dmpm})_2Cl_2$ (**3**), $Au^IRh^I(^tBuNC)_2(\mu\text{-tfepm})_2Cl_2$ (**4**), and $Au^IRh^I(^tBuNC)_2(\mu\text{-tfepma})_2Cl_2$ (**5**) were synthesized and **2**, **3**, and **5** were crystallographically characterized. Absorption spectra at room temperature, excitation spectra, emission spectra, and phosphorescence lifetimes of glass-solution and solid state samples at 77 K are reported for **2-5** and interpreted in context of crystallographic structure, electronic structure, and time-dependent density functional theory (TD-DFT) calculations. **2-5** are intensely luminescent at 77 K, with **4** and **5** exhibiting "dual emission."

Thesis Supervisor: Daniel G. Nocera

Contents

List of Figures

List of Tables

(Main text only)

Crystallographic data were produced by David R. Manke

DFT calculations were performed by Arthur J. Esswein

1 Introduction

With the demand for harnessed energy rising and the supply of expendable fossil fuels decreasing, the need for alternative fuel sources is of paramount importance. Members of the scientific community have begun to focus their efforts towards exploring these alternative energy sources. In order to develop an efficient and productive energy resource from the earth's abundant renewable fuel sources, the scientific community must first fully comprehend the science involved. It has been recognized that most renewable energy sources are not abundant enough to provide for the earth's rising energy demand, save solar energy and possibly fusion. While sunlight is a wealthy enough resource to utilize, there remains much to be developed in order to truly harness light as an efficient energy supply. Solar energy must be stored in a manner amenable to widespread utilization—and thus the production of a viable fuel such as hydrogen from the sun's energy is imperative.

Normally, a catalyst helps promote an overall downhill reaction by decreasing a large kinetic barrier, allowing the process to proceed thermally. Alternatively, a photocatalyst helps drive an uphill reaction by promoting a reactant into an excited state, allowing the reaction to proceed in an exothermic manner from this energetically elevated state, as seen in Figure 1.

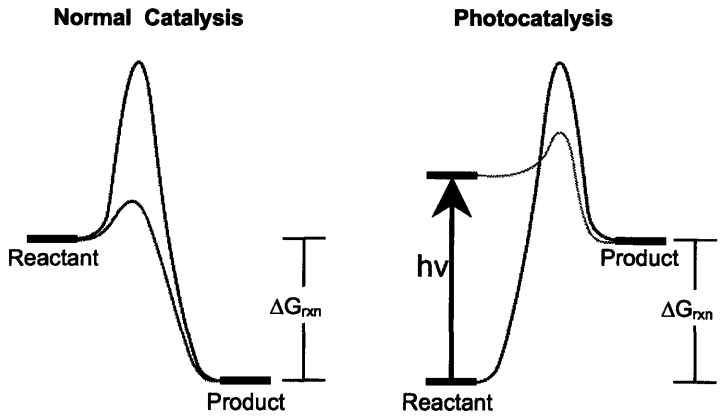

Figure 1. Energy diagram representations of normal catalysis and photocatalysis.

The prospect of utilizing light and a photocatalyst to promote an overall uphill process through excited state reactivity is of particular interest in the context of energy. Ideally, a transition-metal catalyst could be used to store the energy of the sun in chemical bonds. Reactions that are promising in this regard include splitting of water or hydrohalic acids to their elemental precursors. In our proposed scheme, pictured below (Scheme 1), a bimetallic transition-metal photocatalyst helps convert hydrohalic acid to hydrogen and halogen, yielding energy rich hydrogen fuel for use as expendable energy. The photon is used here to activate the high energy metal-halogen bonds, reducing the metal and producing X_2.

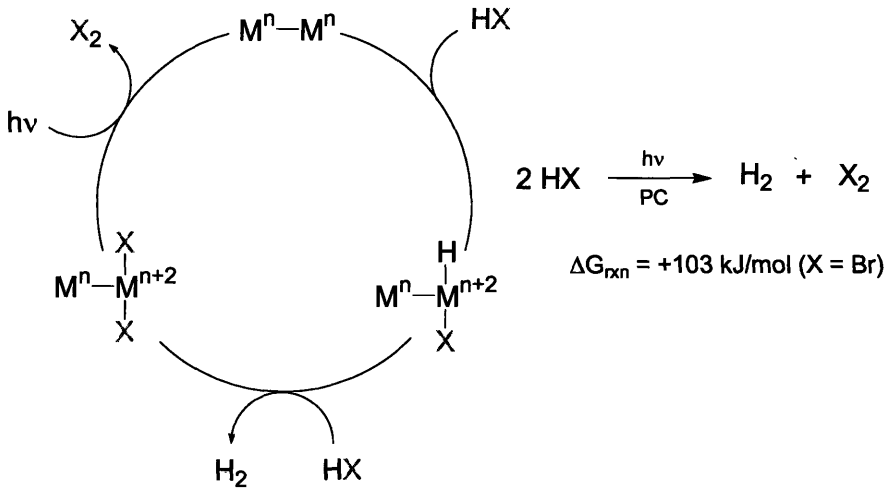

Scheme 1. Proposed catalytic scheme for conversion of hydrohalic acid to hydrogen and halogen.

Another key component of the proposed catalytic cycle is the two-electron mixed valency. As illustrated, the oxidation of the bimetallic transition metal catalyst produces a two-electron mixed-valent complex. This two-electron mixed valency is key in controlling the multielectron chemistry of hydrogen production, as the desired reactivity can occur exclusively in discrete two-electron steps. This helps avoid the common and confining single electron steps usually observed in synthetic chemistry and instead yields a complex whose reactivity more closely mimics the multi-electron reactivity more commonly seen in nature.

Nocera and coworkers have identified a photo-catalytic cycle which produces hydrogen from hydrohalic acid.[1,2,3] A binuclear rhodium complex reacts with HX (X=Cl, Br) to produce H_2 and two metal halogen bonds. The energetic barrier for halogen elimination is overcome by initially photoactivating the complex into its excited state. The elucidated

mechanism of the cycle is seen in Figure 2. The bis-(bis(trifluoroethoxy)phosphino)methyl amine ligand has been abbreviated to the "PNP" backbone for clarity. In the first step of the cycle, a labile ligand, "L" is displaced by two equivalents of HX to oxidize the Rh^0–Rh^0 species to Rh^{II}–Rh^{II}. The halogen atoms add in the axial positions, while the hydrides join syn-equatorial positions. Exposure of this intermediate to light eliminates hydrogen in an efficient manner. The resulting intermediate involves the transition of Rh^I–Rh^I dihalide to the Rh^0–Rh^{II} dihalide mixed valent species. The metal-halogen bonds of this mixed valent species are then photoactivated to eliminate halogen with a quantum yield of 0.1-1%.

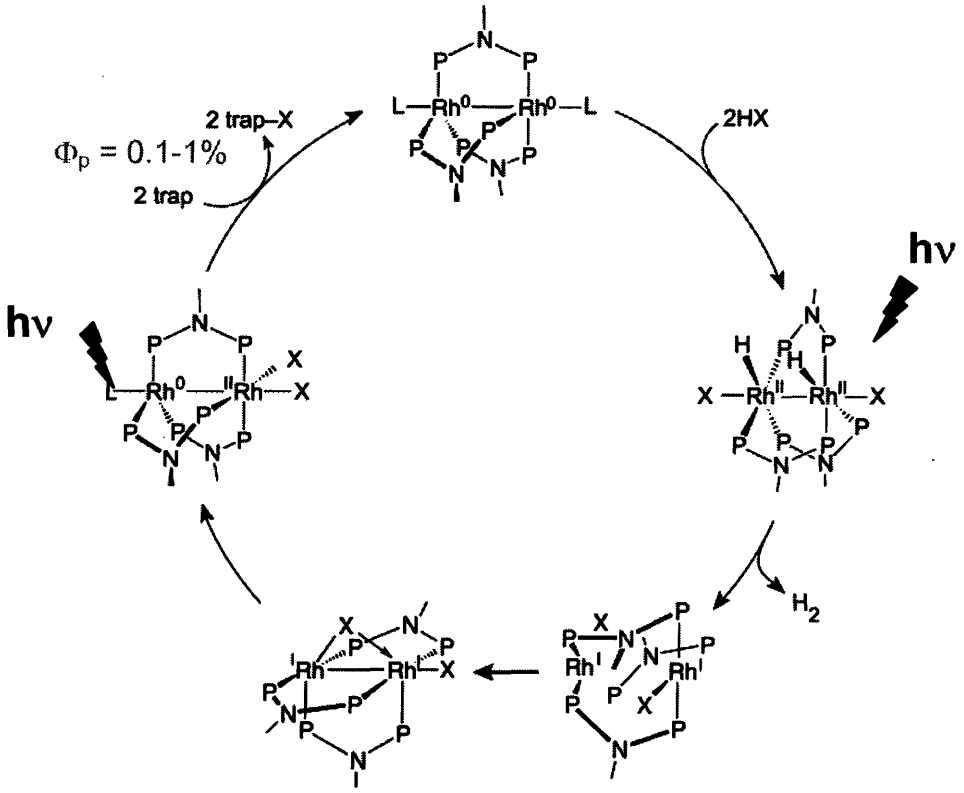

Figure 2. Elucidated mechanism of the production of hydrogen and halogen from HX by a dimeric rhodium catalyst.

Unfortunately, in the case of the rhodium systems developed, photoelimination is only possible in the presence of a halogen radical trap and with a UV photon. Even more important, however, is the low quantum yield of halogen elimination step: 0.1-1%. The activation of the metal-halogen bond is the critical determinant to the overall efficiency of the photocycle and thus hydrogen production. To address this poor photoefficiency, we sought a more strongly oxidizing metal center which could facilitate the activation of M—X bonds.

Gold has been identified as promising for efficient metal-halogen bond activation, because highly oxidized gold(III) species possess redox properties which indicate potential for competent photochemical halogen elimination. Additionally, the tendency for gold(I) and gold(III) species to prefer linear and square planar coordination geometries, respectively,[4] indicates promise for the interconversion between the expected gold(I) and gold(III) hydrohalide and gold(III) dihalide intermediates of the proposed catalytic cycle.

After an initial exploration of dimeric gold species, described within, an interest was aroused in combining the oxidizing properties of gold and the tendency of rhodium to promote facile hydrogen production.[5] The pursuit of a heterobimetallic system capable of closing the catalytic cycle led to the synthesis of a series of heterobimetallic gold(I)-rhodium(I) complexes which possess fascinating photo-luminescent properties at low temperatures. The opportunity to explore the nature of the excited state of these species was exploited, and this thesis herein describes the synthesis and structural characteristics of several heterobimetallic gold(I)-rhodium(I) species, as well as a photo-physical investigation into the electronic structure of their photo-activated excited states.

2 Results and Discussion

2.1 Synthesis and Structure of $Au_2(tfepm)_3Cl_2$

The bis(bis(trifluoroethoxy)phosphino)methane ligand (tfepm), similar to the bis(bis(trifluoroethoxy)phosphino)methyl amine ligand (tfepma) shown to support M^n—M^{n+2} mixed valency in rhodium and iridium compounds,[6] was introduced to gold in an attempt to synthesize a gold dimer with analogous oxidation properties.

An initial synthesis sought to combine the tfepm ligand with a common gold starting material, chloro(triethylphosphine)gold(I) (Scheme 2). The ^{1}H-NMR spectrum of the resulting product consisted of 4 distinct peaks, instead of the two expected. Two of the peaks resembled those of the gold starting material—a quartet and a triplet in a ratio of 2:3.

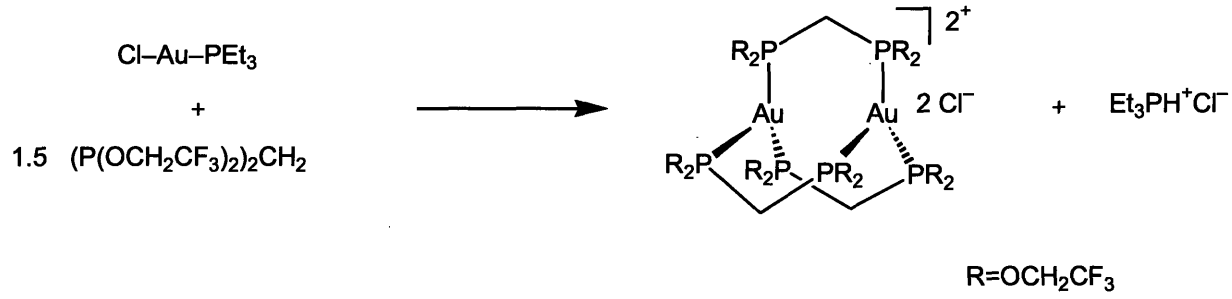

Scheme 2. Synthetic preparation of **1a**.

Crystals of the product were grown from vapor diffusion of pentane into a methylene chlordide solution. The product, $[Au_2(tfepm)_3]Cl_2 \cdot [Et_3PH]Cl$ (**1a**), was elucidated from the crystal structure (Figure 3). Instead of the common linear geometry expected from the di-gold(I) complex synthesized, a rarer coordination geometry was obtained, with gold exhibiting three-coordinate planar geometry. In addition, the complex was co-crystalized with an undesired side-product: [Et3PH]Cl, explaining the two extra proton peaks. The Au—Au distance is 3.5453(9) Å while the Au—Cl distances are 2.771(2) Å and 2.763(2) Å. Crystallographic parameters (Table B1) and a table of selected bond lengths and angles (Table B2) can be found in Appendix 2.

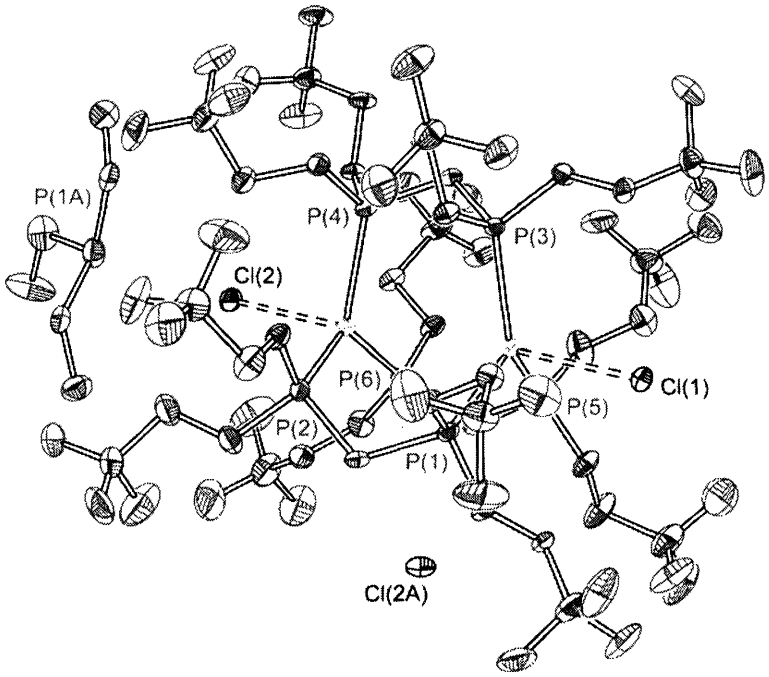

Figure 3. Representation of **1a**, shown as 40% ellipsoids.

A new method of preparation (Scheme 3) utilized chloro(tetrahydrothiophene)gold(I) as a gold precursor and cleanly resulted in solely the gold dimer, $Au_2(tfepm)_3Cl_2$ (**1b**). Notable is the difference in solubility of **1a** and **1b**, as **1a** dissolves readily in chloroform and methylene chloride, while **1b** does not. This synthesis indicates the synthetic flexibility of chloro(tetrahydrothiophene)gold(I), which is not commonly used as a gold precursor for it is not commercially available.

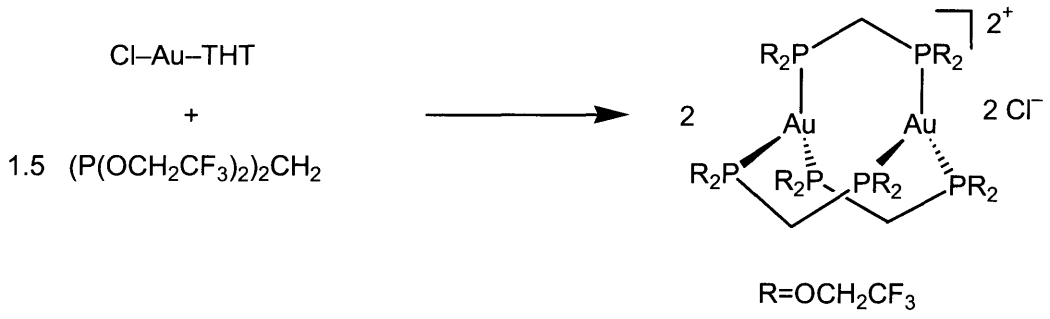

Scheme 3. Synthetic preparation of **1b**.

Single crystals were grown from slow liquid-liquid diffusion of pentane into a tetrahydrofuran solution of **1b**. The geometry of **1b** is almost identical to that of **1a**, with **1b** exhibiting a slightly shorter Au—Au distance of 3.5295(7) Å (Figure 4).

$Au_2(tfepm)_3Cl_2$ is only the second example of a trigonal-planar gold dimer structurally characterized.[7] The Au—Au distances exhibited in **1a** and **1b** are markedly longer than that in the other example, $Au_2(dmpm)_3(BF_4)_2$, which has a Au-Au distance of 3.045 Å. As neither bond length warrants a significant metal-metal interaction, this discrepancy could be due to ligand sterics or the closely associated chloride anions. However, the longer bond length in **1** diminishes the possibility of aurophilic interaction.[8] Crystallographic parameters (Table B1) and a table of selected bond lengths and angles (Table B3) can be found in Appendix 2.

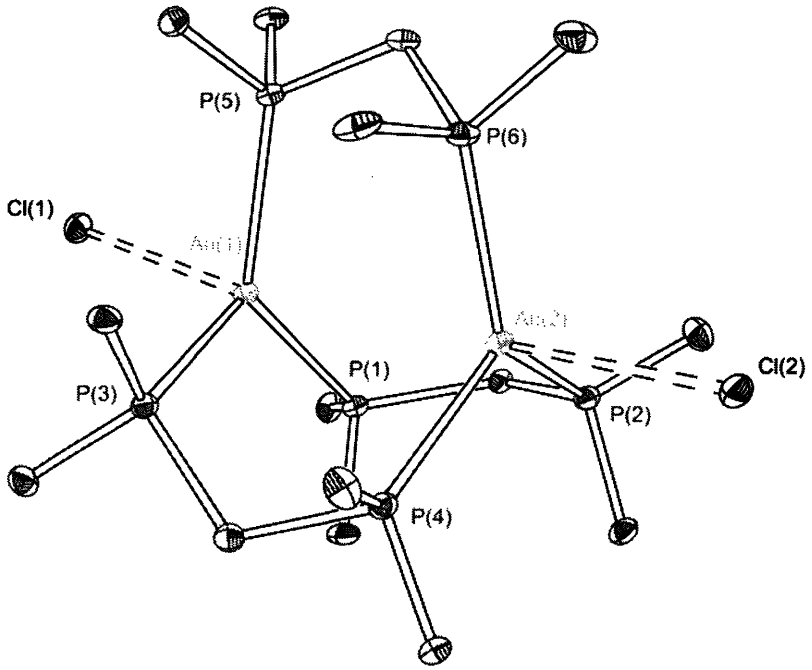

Figure 4. Representation of **1b**, shown as 40% ellipsoids. Trifluoroethoxy groups omitted for clarity.

The unique three-coordinate geometry of **1a** and **1b** is owed to the strongly electron withdrawing nature of the trifluoroethoxy groups, proving the phosphine ligand unable to support gold(I) in its more common linear, two coordinate geometry.

2.2 Synthesis, Structure, and Spectroscopy of Heterobimetallic Gold-Rhodium Complexes

2.2.1 $Au^{I}Rh^{I}(^{t}BuNC)_2(\mu\text{-dppm})_2Cl_2$

A modified synthetic approach to the literature preparation of $Au^{I}Rh^{I}(^{t}BuNC)_2(\mu\text{-dppm})_2(PF_6)_2$ [dppm = bis(diphenylphosphino)methane][9] was developed to prepare $Au^{I}Rh^{I}(^{t}BuNC)_2(\mu\text{-dppm})_2Cl_2$ (**2**) in a one-pot method. Treatment of chloro(1,5-cyclooctadiene)rhodium(I) dimer in dichloromethane with 4 eq. dppm, followed by 4.5 eq. *tert*-butyl isocyanide and 2 eq. of chloro(triethylphosphine)gold(I) generated complex **2** in 66% yield (Scheme 4). The Rh^{I} monomeric species formed before the addition of chloro(triethylphosphine)gold(I) has been characterized by Shaw and coworkers through variable temperature NMR and suggested to consist of three equivalents of dppm per each rhodium coordinated in a monodentate fashion.

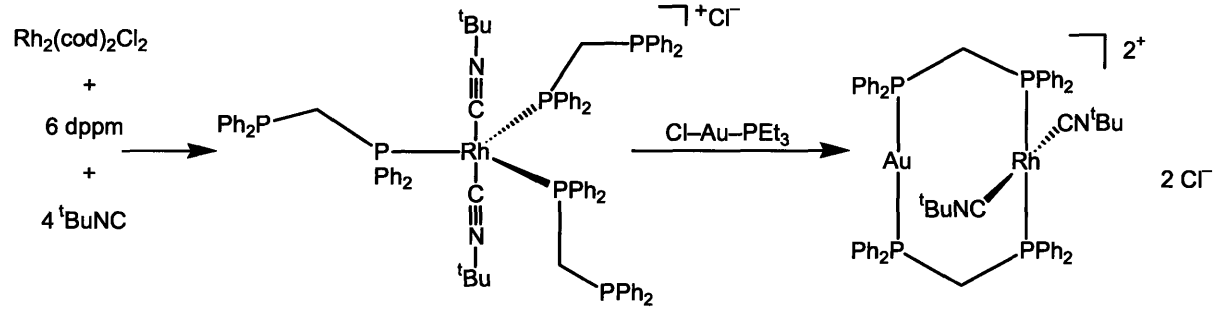

Scheme 4. Synthetic preparation of **2**.

Single crystals were grown by diffusion of diethyl ether into a dichloromethane solution of **2** at room temperature. The previously undetermined crystal structure of the species displays a nearly square planar rhodium(I) center with two trans *tert*-butyl isocyanide groups and two trans μ–bridging dppm ligands to a linear gold center (Figure 5). The Au-Rh interatomic distance is 2.9214(9) Å. This distance is slightly longer than that of the only other known Au–Rh species, $Au^{I}Rh^{I}(\mu\text{-PNP})_2(BF_3NO_3)$ (PNP = 2-[bis(diphenylphosphino)methyl]pyridine), reported as 2.850(2) Å.[10] The P-Au-P angle of **2** is nearly linear at 174.99°, as is the P-Rh-P angle, at

173.01°. The chloride anions are not associated to the metal centers. Crystallographic parameters (Table B1) and selected bond lengths and angles (Table B4) are tabulated in Appendix 2.

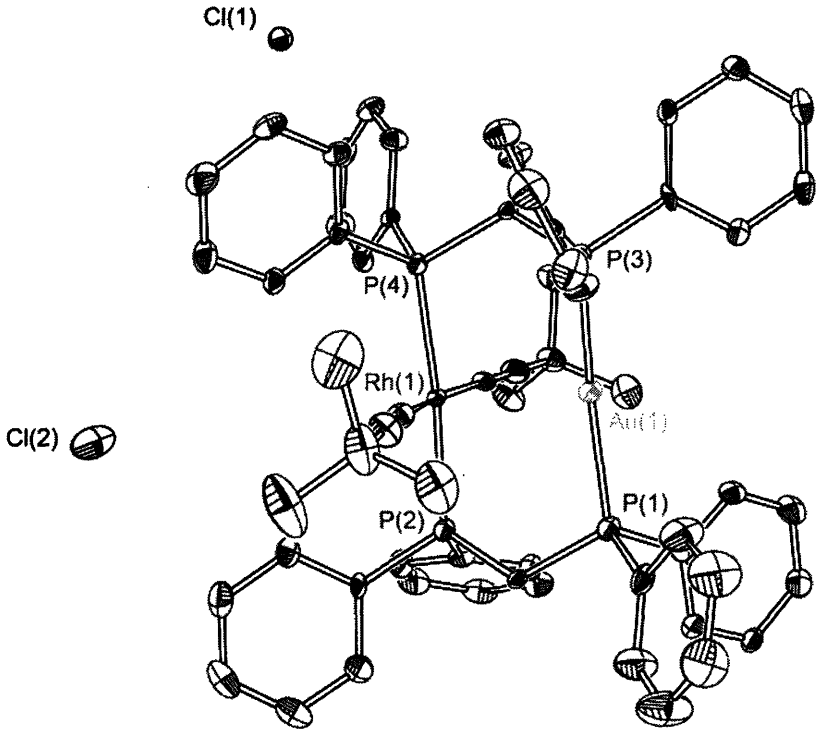

Figure 5. Representation of $Au^{I}Rh^{I}(^{t}BuNC)_2(\mu\text{-dppm})_2Cl_2$ (**2**), shown as 40% ellipsoids.

The room temperature absorbance spectrum of **2** is presented in Figure 6. Absorption maxima are seen at 456 nm (ε_{max} = 20,266 M^{-1} cm^{-1}) and 340 nm (ε_{max} = 7,391 M^{-1} cm^{-1}).

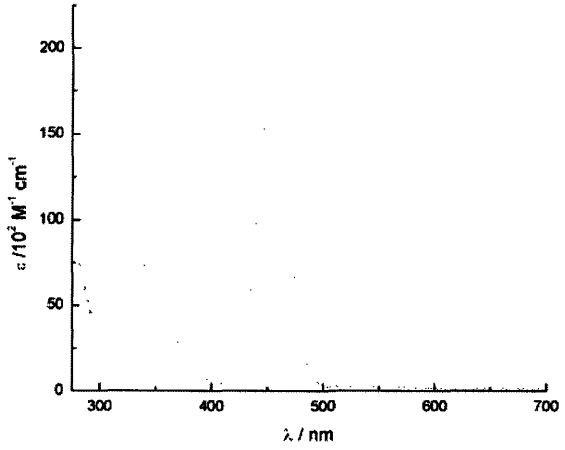

Figure 6. Room temperature absorbance spectrum of an ethanol solution of **2.**

Emission (λ_{ex} = 460nm) and excitation (λ_{em} = 617 nm) spectra for **2** measured in a 77 K glassy-ethanol solution are seen in Figure 7. Two emission bands, centered at 495 nm and 621 nm are seen in the glassy solution. The intense emission is visible to the eye, as the glass solution appears bright red in color when excited. These spectral measurements are in agreement with Che coworkers[11] and Crosby and coworker,[12,13] who assign the two bands as fluorescence and phosphorescence, arising from the $^1(d\sigma^* \rightarrow p\sigma)$ and $^3(d\sigma^* \rightarrow p\sigma)$ states, respectively. The spectral measurements of **2**, measured in the solid state (λ_{ex} = 449 nm, λ_{em} = 665 nm), are plotted in Figure 8. The solid emission is intensely red in color. Only a single broad emission band is observed at 665 nm and is attributed to the phosphorescence. This red shift in the solid was not observed in the experiments performed by Che and coworkers.

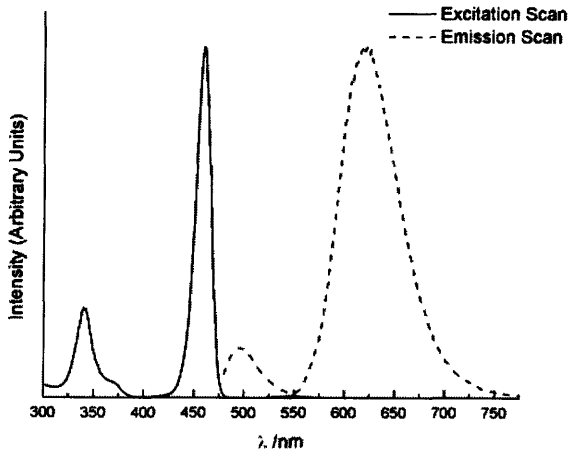

Figure 7. 77K emission and excitation spectra of **2**, ethanol glass solution. λ_{ex} = 460 nm, λ_{em} = 617 nm.

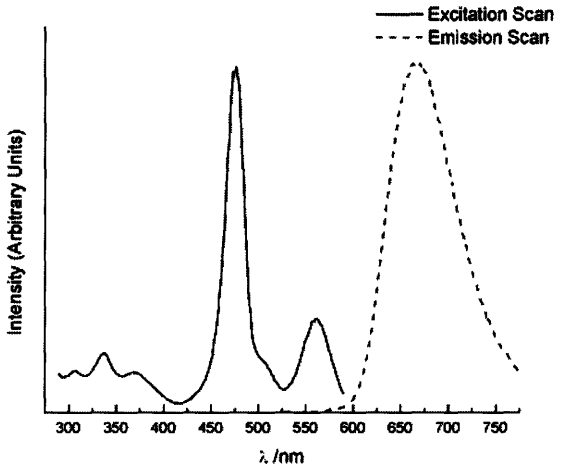

Figure 8. 77K emission and excitation spectra of **2**, solid state. λ_{ex} = 475 nm, λ_{em} = 665 nm.

The excitation spectrum in the glass solution consists of bands at 340, 459, and 557 nm. In agreement with Che and coworkers, the last two bands are assigned to the $^1(d\,\sigma^* \rightarrow p\sigma)$ and $^3(d\,\sigma^* \rightarrow p\sigma)$ transitions, respectively, and the high energy band is attributed to a $^1(d_{yz}(Rh) \rightarrow p\sigma)$ transition. In the solid state, excitation bands (λ_{emit} = 665) are observed at 306, 336, and 476, and 561 nm, with the 561 nm band being proportionally much more intense in the solid state than in the glass solution.

Based on the treatment of the electronic structure of $Au^IRh^I(^tBuNC)_2(\mu\text{-dppm})_2(ClO_4)_2$ species by Che et al, and the results obtained here, a qualitative molecular orbital diagram for $[Au^IRh^I(^tBuNC)_2(\mu\text{-dppm})_2]^{2+}$ was derived (Figure 9). The highest occupied molecular orbital (HOMO) is identified as the $d\sigma^*$ antibonding interaction between the d_{z2} orbitals of Rh and Au, while the lowest unoccupied molecular orbital (LUMO) is the $p\sigma$ bonding interaction between the metal p_z orbials. Che and coworkers describe the LUMO as having mixed p_z(Rh) and π^*(isocyanides and phosphines) in addition to the metal-metal p_z interaction, thus localizing the LUMO on rhodium. Crosby and coworker, however, cite the LUMO to be primarily localized on a gold $6p_z$ orbital.

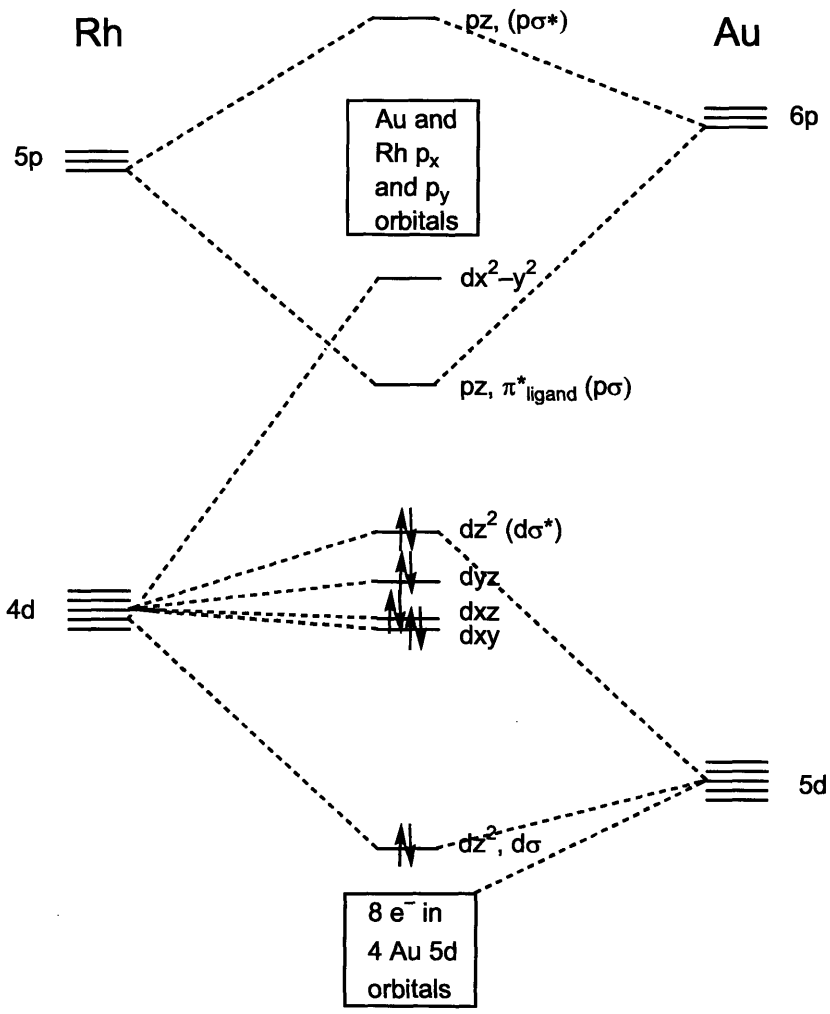

Figure 9. Qualitative molecular orbital diagram of **2.**

A time dependent density functional theory (TD-DFT) calculation was performed on the related species $[Au^{I}Rh^{I}(MeNC)_2(\mu\text{-dmpm})_2]^{2+}$ (dmpm = bis(dimethylphosphino)methane). The TD-DFT calculated singlet transition energies were calculated and determined to be those belonging to HOMO → LUMO, HOMO → $LUMO^{+1}$, and $HOMO^{-1}$ → LUMO transitions, and are tabulated in Table C3. Pictorial representations of the orbitals involved are pictured in Figure 10. The HOMO → LUMO transition is calculated to be 482 nm, in agreement with observed. As expected, the HOMO is solely dσ* in character. The pσ bonding character between rhodium and gold is observed in the LUMO, but orbital is primarily rhodium based π* interactions with the isonitrile ligands. Two higher energy transitions are calculated at 385 nm and 376 nm and attributed to the HOMO → $LUMO^{+1}$ and $HOMO^{-1}$ → LUMO transitions, respectively. Only one

transition is observed experimentally in **1**, but one could note the asymmetry of the band as arising from two energetically similar transitions. The $HOMO^{-1}$ is almost exclusively rhodium d_{yz} in character, while the $LUMO^{+1}$ consists of Au—P π interactions. The rhodium localized HOMO → LUMO transition suggested by Che et al is supported by these calculations. Further computational details are provided in Appendix 3.

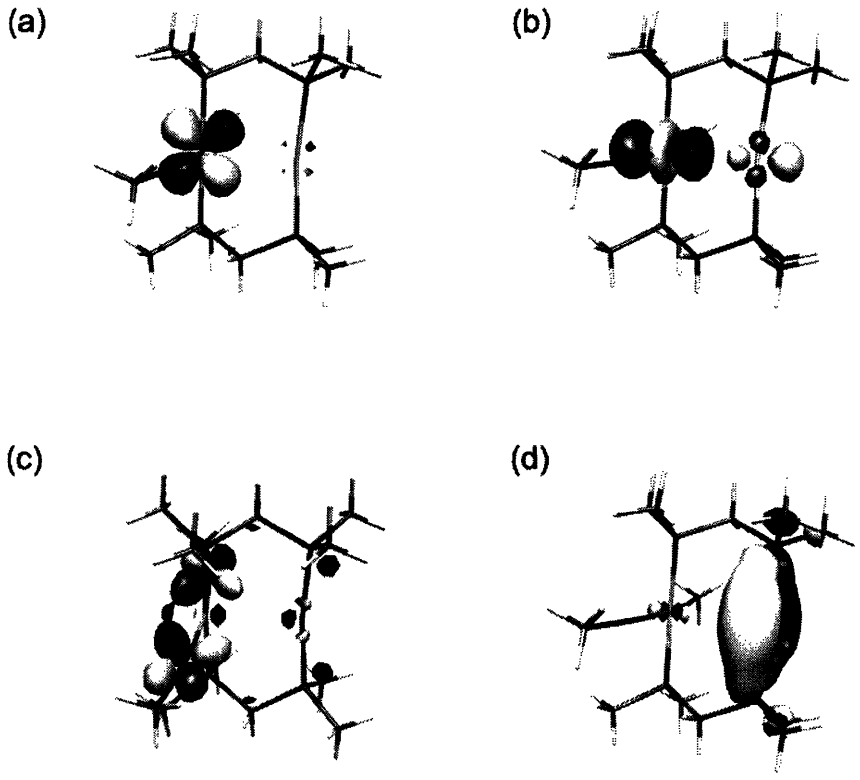

Figure 10. Molecular orbital pictures of the a. $HOMO^{-1}$, b. HOMO, c. LUMO, and d. $LUMO^{+1}$ of $[Au^{I}Rh^{I}(MeNC)_2(\mu\text{-dmpm})_2]^{2+}$.

As noted above, the fluorescence and phosphorescence of **2** correspond to the singlet and triplet $p_z\sigma \rightarrow d_{z2}\sigma^*$ transitions. The observed lifetime of the triplet excited state is 15.8 μs in glassy-ethanol solution. This data is in agreement with that of Striplin and Crosby, who observed a lifetime of 11.5 μs in glassy-ethanol solution for the corresponding hexafluorophosphate derivative. A biexponential fit was performed to determine the solid-state lifetime and with τ_1 = 12.6 (57%) μs and τ_2 = 3.58 μs (43%). The fluorescence lifetime was unable to be measured on our nanosecond laser system.

2.2.2 Synthesis and Structure of Novel Au–Rh Complexes

We have sought to expand the synthetic construction of Au—Rh heterobimetallic species beyond the two species formally known in the literature. $Au^{I}Rh^{I}(^{t}BuNC)_2(\mu\text{-dmpm})\ _2Cl_2$ (**3**) [dmpm = bis(dimethylphosphino)methane] was prepared in an analogous manner to **2**, as illustrated in Scheme 5.

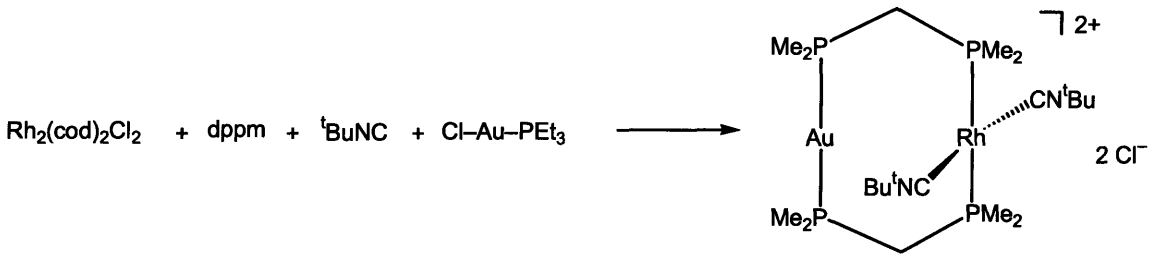

Scheme 5. Synthetic preparation of **3**.

Red single crystals of **3** were grown by slow diffusion of pentane into a methylene chloride solution at room temperature. The crystal structure (Figure 11) displays similar geometry to that of **2**, with a slightly longer Au—Rh interatomic distance of 2.9666(14) Å. The P—Au—P angle is nearly linear at 174.17(15)°, as is the P—Rh—P angle, at 176(17)°. General crystallographic parameters (Table B1a), as well as selected bond lengths and angles (Table B5) can be found in Appendix 2.

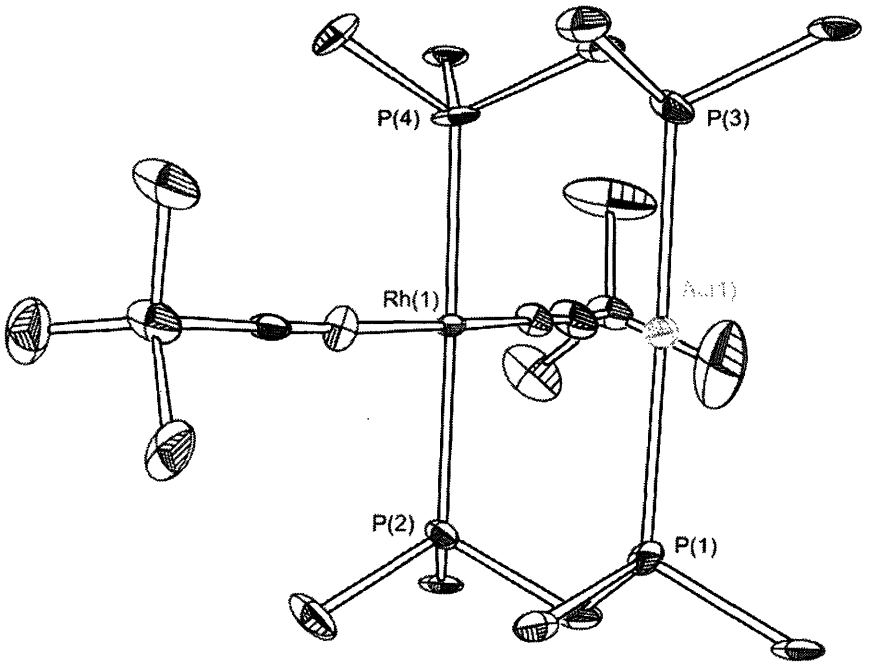

Figure 11. Representation of **3**, shown as 40% ellipsoids. Selected bond lengths and angles tabulated in appendix.

$Au^{I}Rh^{I}(^{t}BuNC)_2(\mu\text{-tfepm})_2Cl_2$ (**4**) [tfepm = bis(bis(trifluoroethoxy)phosphino)methane] was also prepared in an analogous manner to **2**, as seen in Scheme 6.

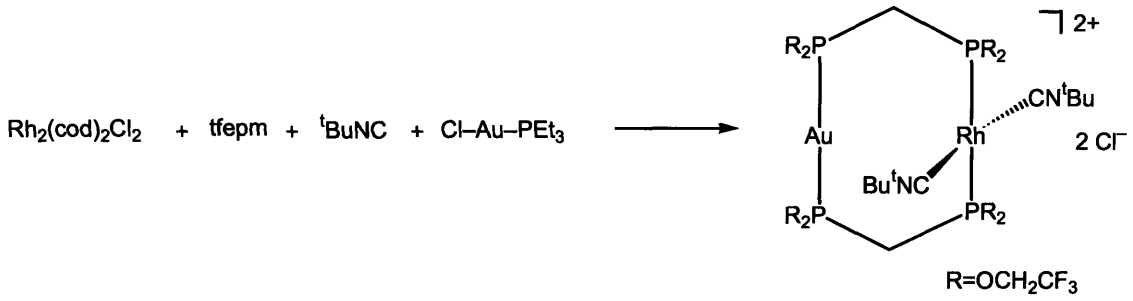

Scheme 6. Synthetic preparation of **4**.

Single crystals of **4** suitable for x-ray diffraction were unable to be obtained. The species was characterized by ^{1}H and ^{31}P NMR. A broad singlet at δ 4.12 ppm is attributed to the protons of the trifluoroethoxy group, while a broad singlet at δ 2.27 ppm is determined to belong to the methylene bridging protons and a singlet at δ 1.39 ppm belongs to the *tert*-butylisonitrile protons. A singlet (δ 31.326 ppm) and a doublet peak (δ 26.434 ppm) observed in the phosphorous NMR belong to the phosphines supporting gold and rhodium, respectively.

$Au^{I}Rh^{I}(^{t}BuNC)_2(\mu\text{-tfepma})\ {}_2Cl_2$ (**5**) [tfepma = bis(bis(trifluoroethoxy)phosphino)methyl amine] was prepared in an a similar manner to **2** (Scheme 7), with the use of chloro(tetrahydrothiophene)gold(I) instead of chloro(triethylphosphine)gold(I).

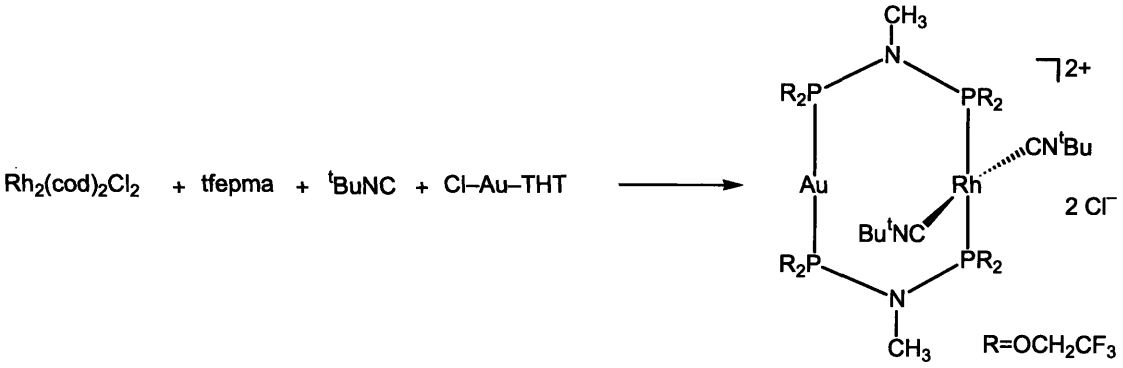

Scheme 7. Synthetic preparation of **5**.

Single yellow crystals were obtained by cooling a methylene chloride / pentane solution of **5** at –40 °C. The Au—Rh interatomic distance of 2.8186(5) Å observed in the crystal structure (Figure 12) is significantly shorter than those observed in **2** and **3**. The chloride anions are closely associated to the metal centers, with Au—Cl and Rh—Cl distances of 2.6564(13) Å and 2.6034(13) Å. The nearly linear P—M—P geometry seen in **2** and **3** is not observed in **5**. The P—Au—P angle is measured to be 151.36(5)° while a P—Rh—P angle of 166.48(5)° is observed. General crystallographic parameters (Table B1a), as well as selected bond lengths and angles (Table B6) can be found in Appendix 2.

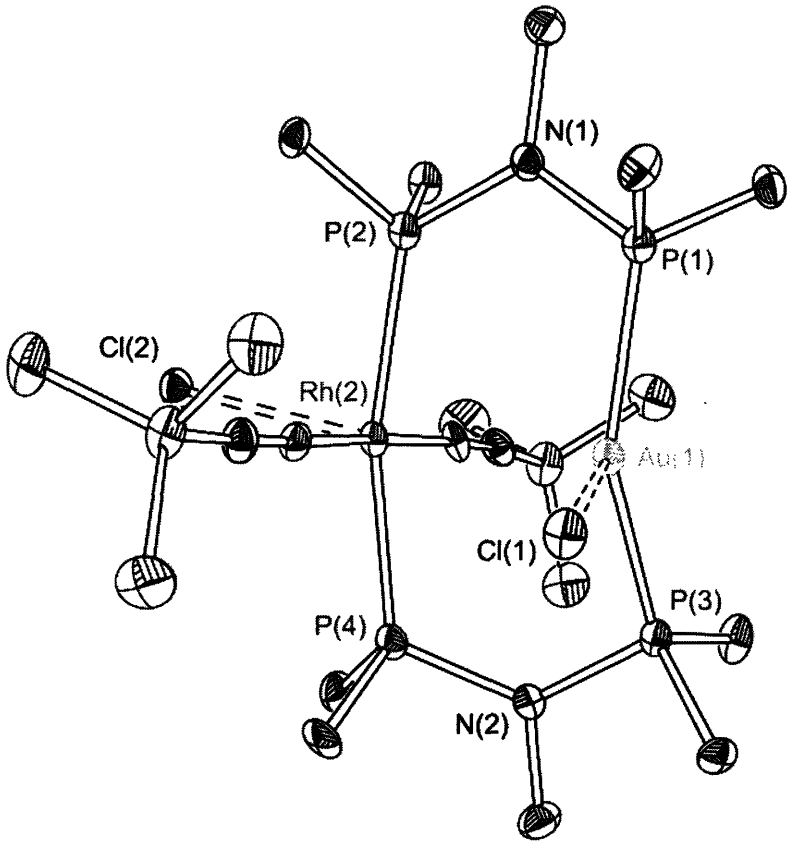

Figure 12. Representation of **5**, shown as 40% ellipsoids. Trifluoroethoxy groups omitted for clarity.

2.2.3 Spectral Investigations of Novel Au–Rh Complexes

With the synthetic expansion of Au—Rh complexes complete, we next extended our photophysical studies to include these new species. The results of these investigations are tabulated and discussed below.

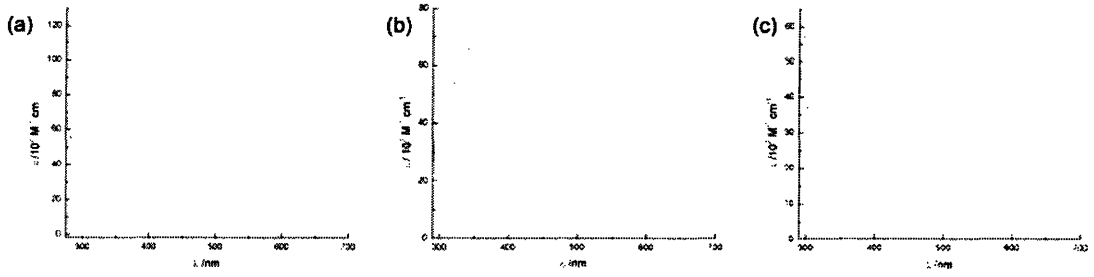

Figure 13. Room temperature absorbance spectra of an ethanol solution of (a) **3**, a THF solution of (b) **4**, and a THF solution of (c) **5**.

The room temperature absorption spectra of **3**, **4**, and **5**, are presented in Figure 13. Band maxima, along with extinction coefficients are reported in Table 1. The methyl analog of **2**, complex **3**, has a similar absorption profile, with the band maxima slightly blue-shifted. The tfepm species, **4**, shows similar profile features, but also has an absorbance shoulder at 298 nm. The tfepma complex, **5**, has a distinct high energy absorbance at 297 nm, and a maxima at 355 nm, but does not show strong absorbance at lower energies.

Table 1. Absorbance data for complexes **2-5**.

Complex	*Solvent*	*Band max, nm (ε, M^1 cm^{-1})*		
$Au^{I}Rh^{I}(^{t}BuNC)_2(\mu\text{-dppm})_2Cl_2$ (**2**)	EtOH	456 (20,266)	340 (7,391)	
$Au^{I}Rh^{I}(^{t}BuNC)_2(\mu\text{-dmpm})_2Cl_2$ (**3**)	EtOH	448 (11,225)	331 (5,512)	
$Au^{I}Rh^{I}(^{t}BuNC)_2(\mu\text{-tfepm})_2Cl_2$ (**4**)	THF	431 (1,890)	336 (6,738)	298 (4,043)
$Au^{I}Rh^{I}(^{t}BuNC)_2(\mu\text{-tfepma})_2Cl_2$ (**5**)	THF		355 (3,696)	297 (5,368)

Emission scans and excitations scans of **3-5** in both glass solutions (Figure 14) and solid states are plotted below. Emission band data and lifetimes are tabulated in Table 2. Complex **3** shows similar photophysical characteristics to **2**, but has blue-shifted excitation and emission. The species emits a deep orange in a glassy-solution and a red-orange in the solid state. The lifetimes of these "red" emissions are comparable. One can hence infer that the assignment made to the transitions in **2**, are applicable to **3**. One salient difference to note occurs in the solid-state excitation spectra of **3**. The lower energy band, at 546 nm, attributed to the $^3(d\ \sigma^* \rightarrow p\sigma)$ transition, becomes the dominant excitation wavelength instead of the $^1(d\ \sigma^* \rightarrow p\sigma)$ transition observed as most intense in the glassy-solution of **3** or the excitation scans of **2**.

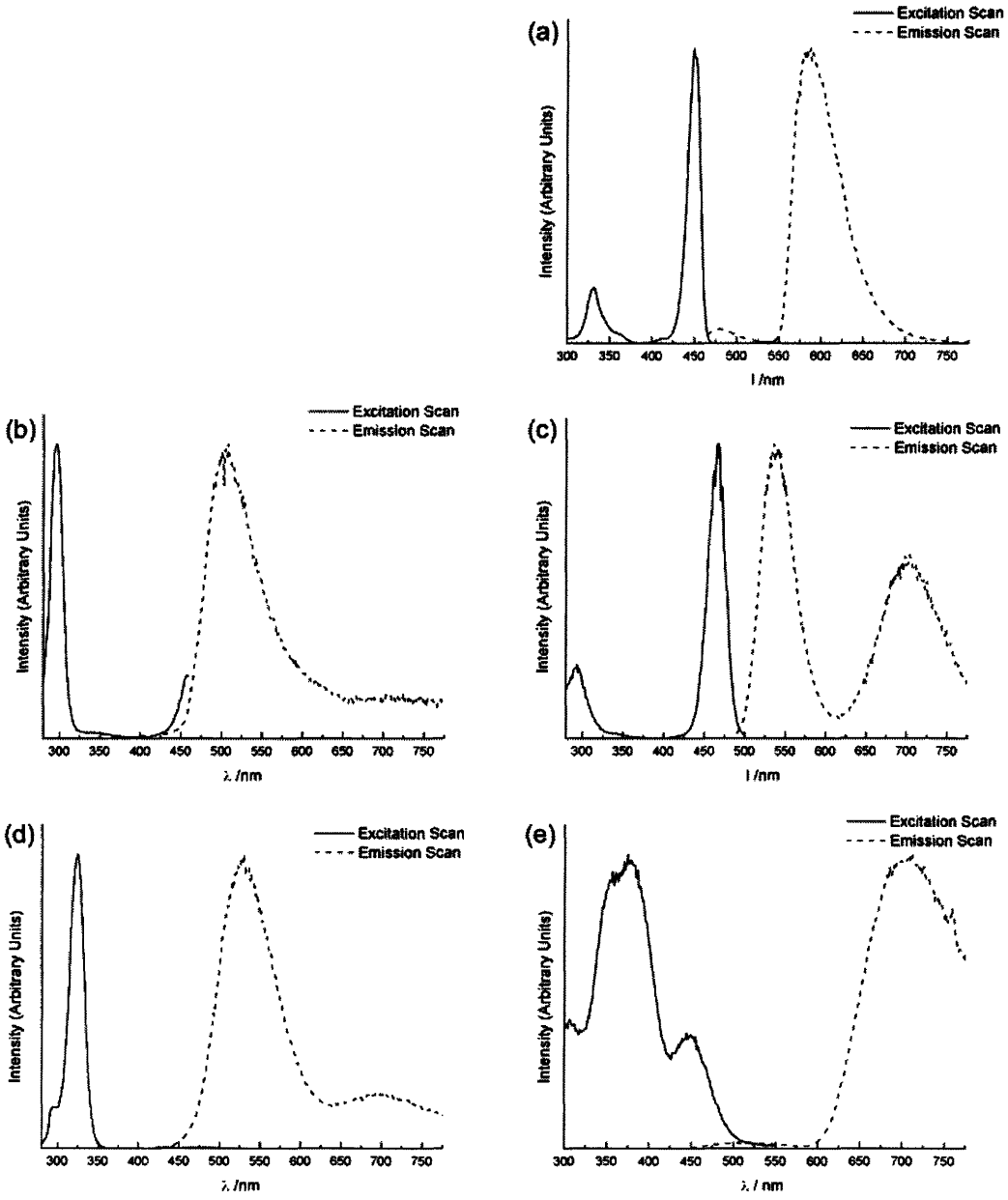

Figure 14. 77K emission and excitation spectra of (a) **3,** ethanol glass solution, λ_{ex} = 449 nm, λ_{em} = 586 nm, (b) **4**, 2-methyl THF glass solution, λ_{ex} = 295 nm, λ_{em} = 505 nm, (c) **4**, 2-methyl THF glass solution, λ_{ex} = 466 nm, λ_{em} = 705 nm, (d) **5**, 2-methyl THF glass solution, λ_{ex} = 325 nm, λ_{em} = 525 nm, (e) **5**, 2-methyl THF glass solution, λ_{ex} = 380 nm, λ_{em} = 705 nm.

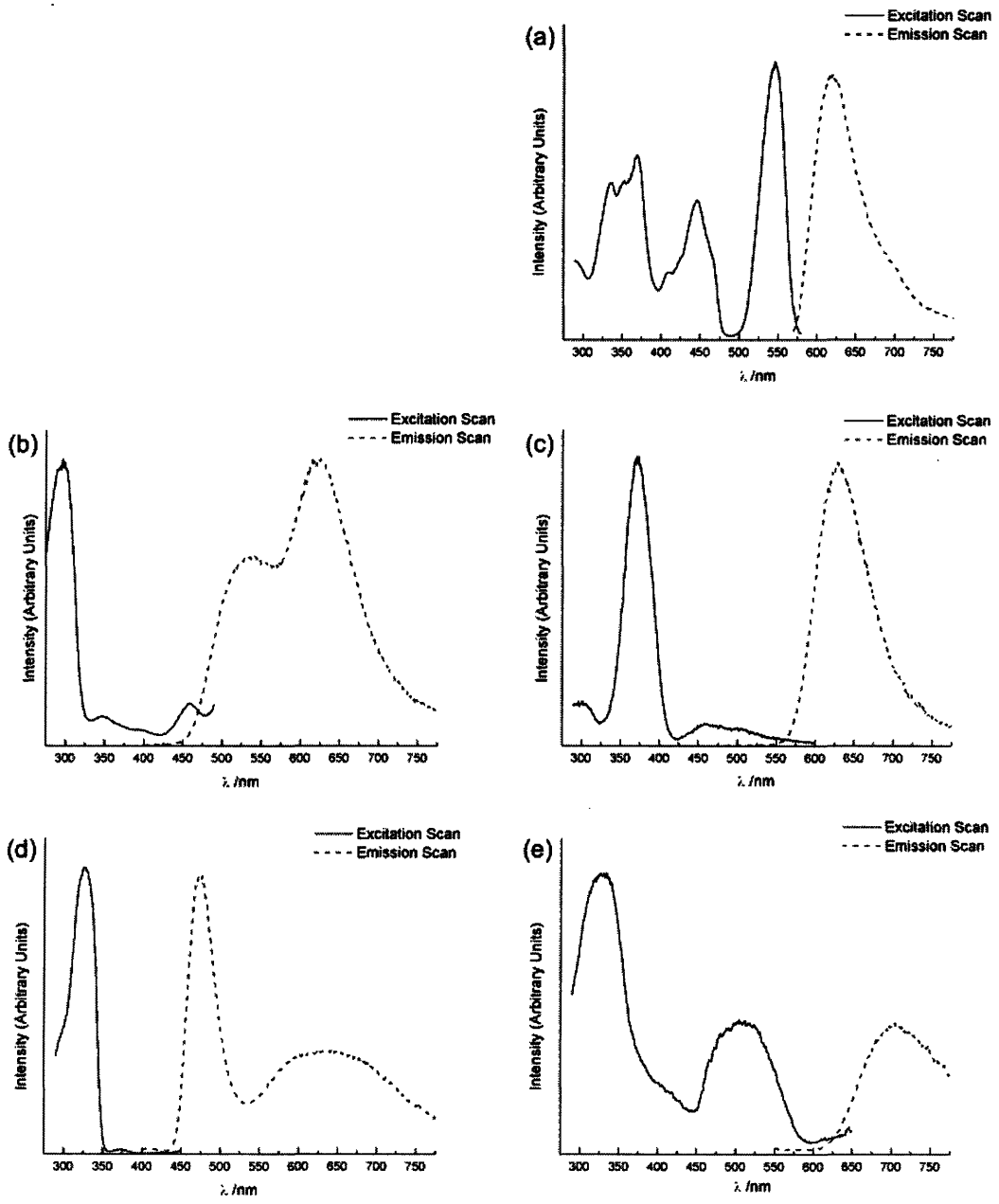

Figure 15. 77K emission and excitation spectra of solid state samples of (a) **3**, λ_{ex} = 447, 545 nm, λ_{em} = 617 nm, (b) **4**, λ_{ex} = 300 nm, λ_{em} = 550 nm, (c) **4**, λ_{ex} = 370 nm, λ_{em} = 630 nm, (d) **5**, λ_{ex} = 325 nm, λ_{em} = 473 nm, (e) **5**, 2-methyl THF glass solution, λ_{ex} = 505 nm, λ_{em} = 705 nm.

Both species **4** and **5** glow a deep red, in a glassy-2-methyl THF solution when excited at 466 and 380 nm, respectively, with emission maxima centered at about 700 nm. The solids of these species also emit red in color, when excited at 370 and 505 nm, respectively. However, when excited at higher energy wavelengths—295 nm for **4** and 325 nm for **5**—the species emit a

fierce green color in the glassy-solution state and a yellow-green color in the solid state. The lifetimes of the "green" bands of **4** and **5**, tabulated below, are significantly shorter than the "red" bands.

Table 2. Emission data for complexes **2-5** taken at 77K.

Complex	*Matrix*	λ_{ex}	*Band max (nm)*	*Lifetime (μs)*
$Au^{I}Rh^{I}(^{t}BuNC)_2(\mu\text{-dppm})_2Cl_2$ (**2**)	EtOH	460	495(f), 621	15.8
	solid	475	665	$\tau_1 = 12.6$ (57%)
				$\tau_2 = 3.58$ (43%)
$Au^{I}Rh^{I}(^{t}BuNC)_2(\mu\text{-dmpm})_2Cl_2$ (**3**)	EtOH	449	479(f), 587	15.0
	solid	447	620	$\tau_1 = 9.76$ (53%)
				$\tau_2 = 2.64$ (47%)
$Au^{I}Rh^{I}(^{t}BuNC)_2(\mu\text{-tfepm})_2Cl_2$ (**4**)	2-MeTHF	295	508	
	2-MeTHF	466	535, 700	
	solid	300	542, 625	($\lambda = 542$)
				$\tau_1 = 0.406$ (62%)
				$\tau_2 = 2.37$ (38%)
	solid	370	628	$\tau_1 = 41.7$ (63%)
				$\tau_2 = 9.46$ (37%)
$Au^{I}Rh^{I}(^{t}BuNC)_2(\mu\text{-tfepma})_2Cl_2$ (**5**)	2-MeTHF	325	529, 712	($\lambda = 529$)
				$\tau = 13.6$
	2-MeTHF	380	707	$\tau = 24.3$
	solid	325	473, 636	($\lambda = 473$)
				$\tau_1 = 9.12$ (51%)
				$\tau_2 = 1.67$ (49%)
	solid	505	704	$\tau_1 = 20.6$ (52%)
				$\tau_2 = 2.89$ (48%)

It is interesting to note that while the glass-solution of **4** appears red in color to the eye when excited at 466 nm, the emission spectrum shows that the "green" 530 nm emission is more intense than the "red" 700 nm band maxima. Excitation at 295 nm of this sample yields sole distinct maxima centered at 508 nm, but the intensity of the right edge of the band peak does not tail off to zero at lower energies. A similar situation is observed for the solid sample of **4**, where the sample appears yellow-green to the naked eye when excited at 300 nm, but the emission scan

consists of two overlapping bands, centered at 542 and 625 nm, with the latter, more red band, greater in intensity.

For species **5**, excitation at lower energies produce sole "red" emission bands centered at 705 nm in both the solid and glass solution states, but excitation at 325 nm yields two bands in both states—the more intense band at the "green" wavelengths and a smaller peak centered at "red wavelengths."

The excitation scans of the "green" bands of **5** isolate a single high-energy wavelength of 325 nm. Excitation of **4**'s "green" band yields the high energy band as the most significant contributor, but small excitation peaks of about 455 nm are observed in the full spectrum. Excitation scans of **4**'s "red" bands identify lower energy peaks as significant contributors to the excited state, but less intense higher energy peaks are also seen. The excitation scan of the "red" band of the glass solution of **5** yields a wide band centered at 374 nm that overlaps two peaks approximately 1/3 the intensity, centered at 300 and 444 nm. The solid state excitation identifies a primary band at 330 nm and a 504 nm band, approximately 40% the intensity. Excitation at 330 nm, as noted above, however, yields visible bright green emission with a band max at 525 nm, and thus excitation at 504 nm is necessary to isolate the red emission.

Table 3. Excitation Scan data for complexes **2-5** taken at 77K.

Complex	*Matrix*	λ_{em}	*Band max, nm (**primary**)*
$Au^{I}Rh^{I}(^{t}BuNC)_2(\mu\text{-dppm})_2Cl_2$ (**2**)	EtOH	617	547, **459**, 340
	solid	665	561, **476**, 308, 338, 368
$Au^{I}Rh^{I}(^{t}BuNC)_2(\mu\text{-dmpm})_2Cl_2$ (**3**)	EtOH	449	542, **449**, 331
	solid	447	**546**, 446, 369
$Au^{I}Rh^{I}(^{t}BuNC)_2(\mu\text{-tfepm})_2Cl_2$ (**4**)	2-MeTHF	505	458, **296**
	2-MeTHF	705	**466**, 294
	solid	550	**296**
	solid	630	**370**
$Au^{I}Rh^{I}(^{t}BuNC)_2(\mu\text{-tfepma})_2Cl_2$ (**5**)	2-MeTHF	525	**325**
	2-MeTHF	705	444, **374**
	solid	473	**325**
	solid	705	504, **330**

A time dependent density functional theory (TD-DFT) calculation was performed on a complex related to **5**, $[Au^{I}Rh^{I}(MeNC)_2(\mu\text{-dfpma})_2]^{2+}$ (dfpma = bis(difluorophosphino)methyl amine). The TD-DFT calculated singlet transition energies were calculated for the HOMO → LUMO, HOMO → $LUMO^{+1}$, and $HOMO^{-1}$ → LUMO and are tabulated in Table C3 (Appendix 3). Pictorial representations of the orbitals involved are pictured in Figure 16. Salient to note are the structural differences between the calculated model and the experimental species, which are tabulated in Appendix 3. The P–M–P angles are nearly linear and the closely associated chloride anions have not been included. The HOMO → LUMO transition is calculated to be 456 nm, in agreement with the 444 nm band observed in the excitation spectra. As expected, the HOMO is solely $d\sigma^*$ in character. The $p\sigma$ bonding character between rhodium and gold is observed in the LUMO, but orbital is primarily rhodium based σ interactions with the isonitrile ligands and the phosphines, unlike the rhodium-ligand π^* interactions seen in the DFT calculations of $[Au^{I}Rh^{I}(MeNC)_2(\mu\text{-dmpm})_2]^{2+}$. Two higher energy transitions are calculated at 389 nm and 375 nm and attributed to the HOMO → $LUMO^{+1}$ and $HOMO^{-1}$ → LUMO transitions, respectively. Neither account for the high energy band observed in the absorption spectra (297 nm) and excitation spectra (325 nm), but are similar in energy to the broad band observed in the excitation spectra of the 707 nm emission.

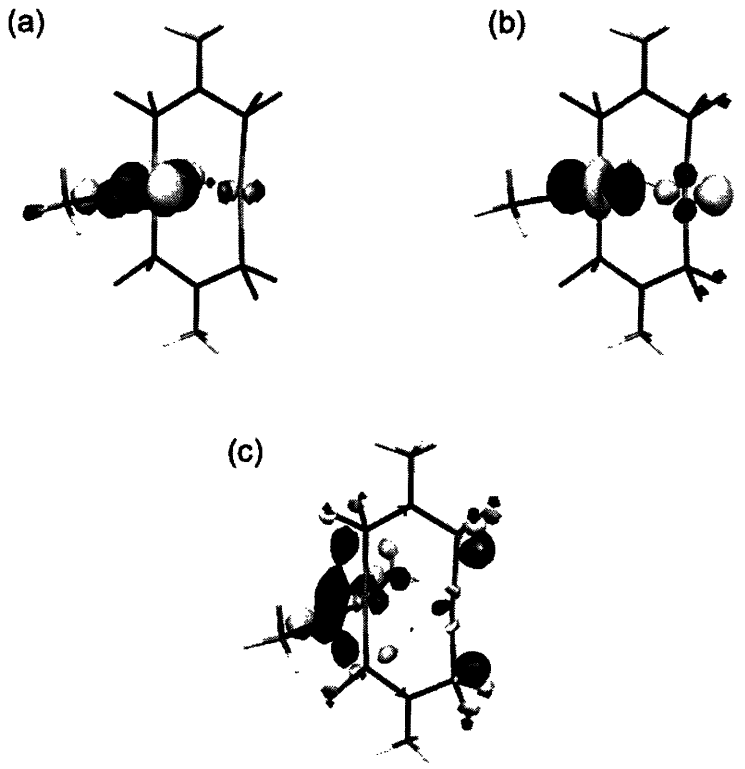

Figure 16. Molecular orbital pictures of the a. $HOMO^{-1}$, b. HOMO, c. LUMO, and of $[Au^{I}Rh^{I}(MeNC)_2(\mu\text{-}dfpma)_2]^{2+}$.

2.2.4 Structural Comparison and Trends in Emission

The nature of the excited state is of paramount importance to the study of photoreactivity in gold–rhodium species. Our experimental investigations have probed both the structure and luminescence of these heterobimetallic species. A direct trend in structural and luminescence characteristics has been observed, and this data gives new experimental evidence for the nature of the excited state.

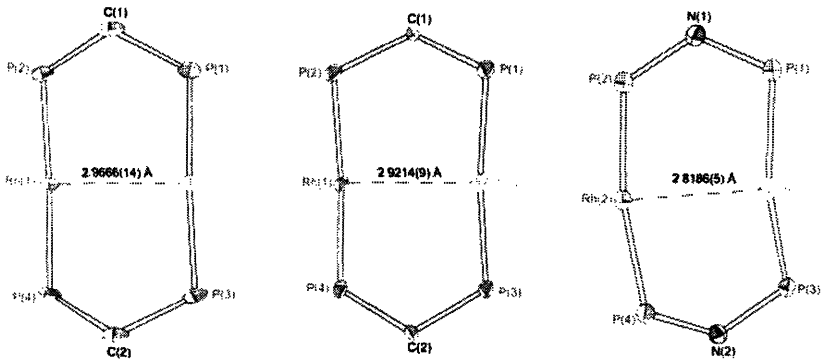

Figure 17. Structural comparison of **2**, **3**, and **5**.

The Au—Rh species bridged by the dmpm ligand (**3**) exhibits the longest interatomic Au—Rh distance and the highest energy "red" emission while the tfepma bridged compound (**5**) exhibits the shortest interatomic distance and the lowest energy "red" emission, as tabulated in Table 4.

Table 4. Comparison of observed interatomic Au—Rh distance and energy of luminescence.

	Au—Rh distance (Å)	$\lambda_{emission}$ *(nm)*
$Au^{I}Rh^{I}(^{t}BuNC)_2(\mu\text{-dmpm})_2Cl_2$ (**3**)	2.9666(14)	587
$Au^{I}Rh^{I}(^{t}BuNC)_2(\mu\text{-dppm})_2Cl_2$ (**2**)	2.9214(9)	621
$Au^{I}Rh^{I}(^{t}BuNC)_2(\mu\text{-tfepma})_2Cl_2$ (**5**)	2.8186(5)	707

As previously described, the nature of the HOMO is primarily dσ* in character, while the LUMO has pσ character. Referring to the abbreviated, qualitative molecular orbital diagram shown in Figure 18, the interaction between the gold and rhodium d orbitals give rise to the dσ* orbital, while the bonding interaction between the empty p_z orbitals on the metals leads to the pσ orbital. A contraction of the interatomic bond distance would increase the interaction between the Au and Rh centers, raising the dσ* orbital in energy, while lowering the pσ orbital, and decreasing the energy gap between the HOMO and LUMO.

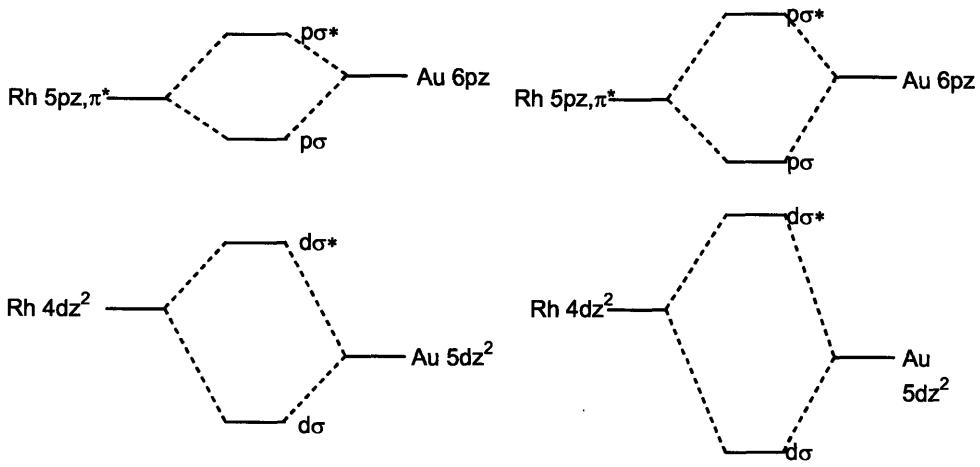

Figure 18. Qualitative Molecular Orbital Diagram illustrating Au—Rh interaction.

The "red" emission observed in the Au—Rh species, as discussed previously, is attributed to the electronic transition from an excited electron in the pσ orbital down to the dσ* orbital. Hence, a smaller energy difference between these two orbitals would result in bathochromic shift of the emission. The experimental evidence presented correlating the interatomic Au—Rh distance with the energy of emission clearly supports the theorized pσ nature of the LUMO, leading us to a better understanding of the nature of the excited state.

2.2.5 High Energy Emission in tfepm and tfepma

The nature of the "red" emission has been characterized in the context of the phosphorescence arising from the ^{3}(dσ*pσ) state, but the character of the high energy "green" emission observed in complexes **4** and **5** has not been fully characterized.

Based on the fact that, when excited at high energy wavelengths, **4** and **5** visibly emit green, but their emission spectra exhibit emission bands at both "red" and "green" wavelengths, it is not unreasonable to think that two interrelated emissive excited states exist.

Alternatively, one could attribute the two emission bands to an isolated rhodium based electronic transition and a gold localized transition. The TD-DFT data shows that the LUMO is localized primarily on the rhodium center for **2**, **3**, and **5**, indicating a likelihood of a rhodium localized excited state. Rhodium(I)-phosphine species tend to emit between 650 and 800 nm,[14,15] which is consistent with the "red" LUMO → HOMO transitions observed in **2-5**. Gold(I)

complexes, however, are usually excited at much higher energies and emit more towards the center of the visible spectrum,[16,17] which is consistent with the observed "green" emission.

There remains, however, the question of why the dual emission is solely observed in the tfepm and tfepma supported Au–Rh complexes and not the others. To truly assign the nature of the dual emission observed in complexes **4** and **5**, more extensive photo physical investigations must be carried out.

Conclusions

A novel trigonal-planar gold dimer (**1a**, **1b**) has been synthesized and structurally characterized. $Au^{I}Rh^{I}(^{t}BuNC)_2(\mu\text{-dppm})_2Cl_2$ (**2**) has been synthesized and structurally characterized. Thorough photo-physical investigations undertaken on the complex, and the results are in agreement with the PF_6 and ClO_4 analogues reported in the literature. The synthesis of Au–Rh heterobimetallic complexes has been expanded to include μ-bridging dmpm, tfepm, and tfepma ligands (**3-5**). **3** and **5** are structurally characterized. All these species are remarkably emissive at 77K, both in glasses and the solid state and their emission spectra, excitation spectra and lifetimes have been recorded. The trends in emission have been correlated to the Au–Rh bond distance of the respective species, elucidating the pσ nature of the photo-excited state. TD-DFT calculations elucidate the nature of the electronic transitions and calculations propose that the LUMO is both Au–Rh pσ and Rh-ligand π* in nature. The use of trifluoroehtoxy substituted phosphine ligands (tfepm and tfepma) yields dually-emissive compounds that, depending on the wavelength of excitation, visibly emit green or red in color. The nature of the green emission has been speculated, but further investigations are required to understand its character.

References

(1) Heyduk, A.F.; Nocera, D.G. *Science* **2001**, *293*, 1639-1641.

(2) Heyduk, A.F.; Macintosh, A.M.; Nocera, D.G. *J. Am. Chem. Soc.* **1999**, *121*, 5023-5032.

(3) Gray, T.G.; Veige, A.S.; Nocera, D.G. *J. Am. Chem. Soc.* **2004**, *126*, 9670-9678.

(4) See Greenwood, N.N.; Earnshaw, A. p. 1187-1196 in *Chemistry of the Elements* Pergamon Press, NY, 1984.

(5) Esswein, A.J.; Veige, A.S.; Nocera, D.G. *J. Am. Chem. Soc.* **2004** submitted for publication.

(6) Heyduk, A.F.; Nocera, D.G. *J. Am. Chem. Soc.* **2000**, *122*, 9415-9426.

(7) Bensch, W.; Prelati, M.; Ludwig, W. *J. Chem. Soc., Chem. Commun.* **1986**, 1762.

(8) Schmidbaur, H. *Chem. Soc. Rev.* **1995**, 391.

(9) Langrick, C.R.; Shaw, B.L. *J. Chem. Soc. Dalton Trans.* **1985**, 511-516.

(10) McNair, R.J.; Nilsson, P.V.; Pignolet, L.H. *Inorg. Chem.* **1985**, *24*, 1935-1939.

(11) Yip, H.; Lin, H.; Wang, Y.; Che, C. *Inorg. Chem.* **1993**, *32*, 3204-3407.

(12) Striplin, D.R.; Crosby, G.A. *J. Phys. Chem.* **1995**, *99*, 11041-11045.

(13) Striplin, D.R.; Crosby, G.A. *J. Phys. Chem.* **1995**, *99*, 7977-7984.

(14) Fordyce, W.A.; Crosby, G.A. *J. Am. Chem. Soc.* **1982**, *104*, 985-988.

(15) Fordyce, W.A.; Crosby, G.A. *Inorg. Chem.* **1982**, *21*, 1455-1461.

(16) McCleskey, T.M.; Gray, H.B. *Inorg. Chem.* **1992**, *31*, 1733-1734.

(17) King, C.; Wang, J.-C.; Khan, M.N.I.; Fackler, J.P. *Inorg. Chem.* **1989**, *28*, 2145-2149.

A Appendix 1—Experimental Section

A.1 General Considerations

Unless otherwise stated, synthetic manipulations were carried out in a dry, anaerobic environment provided by a nitrogen-filled Vacuum Atmosphere HE-553-2 glovebox. Solvents for synthesis were of reagent grade or better, purchased from VWR, and were purified and dried using a Braun solvent purification system. Elemental analyses were performed by H. Kolbe Mikroanalytisches Laboratorium (Mülheim an der Ruhr, Germany).

$CDCl_3$, CD_2Cl_2, CD_3CN were purchased from Cambridge Isotope Laboratories, sealed under argon and used without further degassing. ^1H NMR and ^{31}P NMR spectra were recorded on a Varian 300 MHz instrument, with shifts reported relative to the residual solvent peak.

The starting materials chloro(1,5-cyclooctadiene)rhodium(I) dimer, bis(diphenylphosphino)methane, bis(dimethylphosphino)methane, ^{t}Butyl isocyanide, and chloro(thiethylphosphine) gold(I) were used as received. Bis(bis(trifluoroethoxy))phosphino methyl amine,[1] bis(bis(trifluoroethoxy)phosphino)methane,[2,3] and chloro(tetrahydrothiophene)gold(I)[4] were prepared according to literature methods.

A.2 Synthesis

Dichlorotris[μ-(bis(bis(trifluoroethoxy)phosphino)methane)]digold(I)•[triethylphosphine chloride] (1a). In a 20 mL scintillation vial, wrapped in foil to shield light, chloro(triethylphosphine)gold(I) (0.150 g, 0.428 mmol) was combined with 1.5 equivalents of bis(bis(trifluoroethoxy)phosphino)methane (0.303 g, 0.640 mmol) in THF (10 mL). The reaction was left to stir for 2.5 h. A clear solution was placed under vacuum to remove solvent to yield a white powder. Single crystals were grown by vapor diffusion of pentane into a methylene chloride solution of **1a** at room temperature. ^1H NMR ($CDCl_3$, 298 K): δ 4.383 (bs, 24 H), δ 2.45 (s, 6 H), δ 1.960 (q, 6 H, J = 7.2 Hz), δ 1.206 (t, 9 H, J = 6.9 Hz).

Dichlorotris[μ-(bis(bis(trifluoroethoxy)phosphino)methane)]digold(I) (1b). In a 20-mL scintillation vial, wrapped in foil to shield light, chloro(tetrahydrothiphene)gold(I) (0.284 g, 0.883 mmol) was treated with 1.5 equivalents of bis(bis(trifluoroethoxy)phosphino)methane (0.625 g, 1.324 mmol) in dichloromethane (8 mL). A white precipitate was formed within 20 min, but the reaction was left to stir for 2 h. The white precipitate was collected by filtration, yielding 0.549 g of **1b** (66%). Single colorless crystals suitable for X-ray structure determination were grown by slow liquid liquid diffusion of pentane into a tetrahydrofuran solution of **1b** at room temperature. ^{1}H NMR (CD_3CN, 298 K): δ 4.835 (multiplet, 24 H), δ 3.264 (s, 6 H) ^{31}P NMR (CD_3CN, 298 K): δ 174.5.

Rhodium(I)gold(I)bis(*tert*-butylisonitrile)bis[μ-bis(diphenylphosphino)methane] dichloride (2). In a 20-mL scintillation vial, wrapped in foil to shield light, cyclobutadiene rhodium(I) chloride dimer (0.100 g, 0.203 mmol) was dissolved in methylene chloride (3 mL) to form an orange solution. While stirring, bis(diphenylphosphino)methane (0.340 g, 0.885 mmol) dissolved in methylene chloride (2 mL) was added dropwise to form a red solution. *Tert*-butyl isocyanide (0.075 g, 0.903 mmol) dissolved in methylene chloride (2 mL) was added dropwise to produce a deep purple-red solution. Next, chloro(thiethylphosphine) gold(I) (0.158 g, 0.451 mmol) dissolved in methylene chloride (2 mL) was added dropwise. The resulting red-orange solution was left to stir for 2 h shielded from light, then diethyl ether (30 mL) was used to precipitate an orange powder. The resulting suspension was filtered, washed with diethyl ether (3 x 20 mL) and dried *in vacuo*, affording **2** as an orange powder, 0.398 g (75%). Red single crystals for X-ray diffraction were obtained by vapor diffusion of ether into a methylene chloride solution of **2**. ^{1}H NMR ($CDCl_3$, 298 K): δ 8.172 (d, *J*=103.2 Hz), δ 7.394 (d, *J*=41.1 Hz), δ 4.887 (bs, 4 H), δ 0.69 (s, 18H). ^{31}P NMR ($CDCl_3$, 298 K): δ 37.095 (m), δ 26.418 (dm, *J*=293 Hz) Anal Calcd for $C_{60}H_{62}AuCl_2N_2P_4Rh$: C 55.19; H, 4.79, N, 2.15. Found: C, 55.11; H, 4.65; N, 2.05.

Rhodium(I)gold(I)bis(*tert*-butylisonitrile)bis[μ-bis(dimethylphosphino)methane] dichloride (3). In a 20-mL scintillation vial, wrapped in foil to shield light, cyclobutadiene rhodium(I) chloride dimer (0.100 g, 0.203 mmol) was dissolved in methylene chloride (3 mL) to form an orange solution. While stirring, bis(dimethylphosphino)methane (0.120 g, 0.885 mmol) dissolved in methylene chloride (2 mL) was added dropwise to form a deep red solution. *Tert*-butyl

isocyanide (0.075 g, 0.903 mmol) dissolved in methylene chloride (2 mL) was added dropwise to produce a very deep purple-red solution. Next, chloro(thiethylphosphine) gold(I) (0.158 g, 0.451 mmol) dissolved in methylene chloride (2 mL) was added dropwise. The resulting red solution was left to stir for 2 h, shielded from light, and then filtered and concentrated *in vacuo*. The resulting red-orange powder was dissolved in methylene chloride (2 mL) and precipitated with pentane (12 mL). The clear supernatant was removed and the product was washed with pentane and dried *in vacuo* yielding **3** as a red-orange powder, 0.176 g (54%). Single red crystals were grown by slow evaporation of a methylene chloride solution of **3** layered under pentane at room temperature. ^{1}H NMR (CD_2Cl_2, 298 K): δ 3.007 (s, 2 H), δ 2.920 (t, *J*=4.68 Hz, 2H), δ 1.84-1.78 (multiplet, 48 H), δ 1.554 (s, 18 H). ^{31}P NMR (CD_2Cl_2, 298 K): δ 9.59 (s), δ 1.743 (d, *J*=203.4 Hz). Anal Calcd for $C_{20}H_{46}AuCl_2N_2P_4Rh$: C 29.68; H, 5.73, N, 3.46. Found: C, 29.62; H, 5.73; N, 3.48.

Rhodium(I)gold(I)bis(*tert*-butylisonitrile)bis[μ-bis(bis(trifluoroethoxy)phosphino)methane] dichloride (4). In a 20-mL scintillation vial, wrapped in foil to shield light, cyclobutadiene rhodium(I) chloride dimer (0.050 g, 0.101 mmol) was dissolved in methylene chloride (3 mL) to form an orange solution. While stirring, bis(bis(trifluoroethoxy))phosphino methane (0.209 g, 0.443 mmol) dissolved in methylene chloride (2 mL) was added dropwise to form a deep red-purple solution. *Tert*-butyl isocyanide (0.038 g, 0.458 mmol) dissolved in methylene chloride (2 mL) was added dropwise to produce a foggy orange solution. Next, chloro(triethylphosphine) gold(I) (0.079 g, 0.225 mmol) dissolved in methylene chloride (2 mL) was added dropwise. The resulting yellow-orange solution was left to stir for 24 h, shielded from light, and then filtered and concentrated *in vacuo*. The resulting yellow oil was redissolved in methylene chloride and precipitated with pentane to yield **5** as a yellow-tan powder. ^{1}H NMR ($CDCl_3$, 298 K): δ 4.12 (bs), δ 2.27 (bs), δ 1.39 (s). ^{31}P NMR ($CDCl_3$, 298 K): δ 31.326 (s), δ 26.434 (d, *J*=195.3 Hz).

Rhodium(I)gold(I)bis(*tert*-butylisonitrile)bis[μ-bis(bis(trifluoroethoxy)phosphino)methyl amine] dichloride (5). In a 20-mL scintillation vial, wrapped in foil to shield light, cyclobutadiene rhodium(I) chloride dimer (0.050 g, 0.101 mmol) was dissolved in methylene chloride (3 mL) to form an orange solution. While stirring, bis(bis(trifluoroethoxy))phosphino methyl amine (0.296 g, 0.609 mmol) dissolved in methylene chloride (2 mL) was added

dropwise to form a green solution that turned yellow with continued addition. *Tert*-butyl isocyanide (0.038 g, 0.458 mmol) dissolved in methylene chloride (2 mL) was added dropwise to produce a dark yellow solution. Next, chloro(tetrahydrothiophene) gold(I) (0.072 g, 0.225 mmol) dissolved in methylene chloride (2 mL) was added dropwise. The resulting orange solution was left to stir for 24 h, shielded from light, and then filtered and concentrated *in vacuo*. The resulting orange oil was dissolved in methylene chloride (2 mL) and an orange powder was precipitated with pentane (15 mL). The clear supernatant was removed and the product was washed with pentane and dried *in vacuo*, yielding **4** as a yellow-orange powder, 0.239 g (78%). Single yellow crystals were obtained by slowly cooling methylene chloride and pentane solution of **4** at -40 °C. ^{1}H NMR ($CDCl_3$, 298 K): δ 4.905 (bs, 4H), δ 4.660 (bs, 8H), δ 4.362 (bs, 4H), δ 2.984 (quintet, J=3 Hz, 6H), δ 1.465 (s, 18H). ^{31}P NMR ($CDCl_3$, 298 K): Anal Calcd for $C_{28}H_{40}AuCl_2F_{24}N_4O_8P_4Rh$: C 22.25; H, 2.67, N, 3.71. Found: C, 22.18; H, 2.54; N, 3.78.

A.3 Physical Methods

Absorption Measurements. UV-visible absorption spectra were recorded on a Spectral Instruments 440 spectrophotometer. Solutions of **2-5** were prepared under aerobic conditions in Starna 7G cells with a 1 cm path length.

General Considerations for Low Temperature Spectroscopy. Glassy-solution samples of **2** and **3** were prepared in ethanol, while those of **4** and **5** were prepared in 2-methyl THF. Solutions were transferred to quartz tubes for measurements under aerobic conditions Solid powder samples of **2**, **3**, **4**, and **5** were sealed under vacuum in quartz tubes. Spectral data were obtained at 77 K by placing quartz tubes in a quartz dewar of liquid nitrogen and aligning sample in excitation path.

Steady-State Luminescence Measurements. Steady-state luminescence data were collected on a Photon Technology International Fluorometer. Data acquisition was performed with FeliX32 software.

Time-Resolved Luminescence Measurements. Time-resolved luminescence data were collected on a nanosecond laser instrument utilizing a Coherent Infinity XPO tunable laser (fwhm = 7 ns) as the source. The Infinity Nd:YAG laser system consisted of an internal diode pumped, Q-switched oscillator, which provided the seed pulse for a dual rod, single lamp, amplified stage. Third harmonic radiation was generated from the Nd:YAG 1064 nm fundamental via Type I polarization and frequency mixing in tuned BBO crystals. The resultant 355-nm beam was passed through a type I tunable XPO to produce the desired excitation wavelength. Sample emission was collected at 90°, to the incident excitation beam by an f/4 collimating lens and was passed onto the entrance slit of an Instruments SA Triax 320 monochromator by an f/4 focusing lens. The signal wavelengths were dispersed by a grating possessing 300 grooves/cm at a blaze wavelength of 500 nm. A wavelength selected signal between, depending on the emission maximum of the sample, was detected by a Hamamatsu R928 PMT. Decay traces were constructed from signals that were averaged for ~1000 scans by a LeCroy 9384CM 1-GHz digital oscilloscope, which was triggered from the Q-switch sync output of the laser. Monochromator operation, data storage, and data manipulation were managed by National Instruments v4.0 driver software (Labview) incorporated into code written at MIT. Communication between a Dell Optiplex GX-1 computer and the instrumentation was achieved through an IEEE-488 (GPIB) interface. Data were fit using Origin 6.0.

References

(1) Heyduk, A. F.; Nocera, D. G. *J. Am. Chem. Soc.* **2000**, *122*, 9415-9426.

(2) Hietkamp, S.; Sommer, H.; Stelzer, O. *Inorg. Synth.* **1989**, *27*, 120-121.

(3) Bitterwolf, T.E.; Raaghuveer, K.S. *Inorg. Chim. Acta* **1990**, *172*, 59-64.

(4) Uson, Rafael; Laguna, Antonio; Laguna, Mariano. *Inorg. Synth.* **1989**, *26*, 85-91.

B Appendix 2–Crystallographic Data

B.1 General Considerations

X-ray diffraction experiments were performed on single crystals grown as noted in synthetic preparations. Crystals were removed from the supernatant liquid and transferred onto a microscope slide coated with Paratone N oil. Selected crystals were affixed to a glass fiber in Paratone N oil and cooled to –123 (**2**) or –173 (**1,3-5**) °C. Data collection was performed by shining Mo Kα (λ = 0.71073 Å) radiation onto crystals mounted onto a Bruker CCD diffractometer. The data were processed and refined by using the program SAINT supplied by Siemens Industrial Automation, Inc. The structures were solved by direct methods (SHELXTL v6.10, Sheldrick, G. M., and Siemens Industrial Automation, Inc., 2000) in conjunction with standard difference Fourier techniques. All non-hydrogen atoms were refined anisotropically unless otherwise noted. Hydrogen atoms were placed in calculated positions. Some details regarding the refined data and cell parameters are provided in Table 1.

B.2 Crystallographic Data

Table B1. Crystallographic data for $[Au_2(tfepm)_3]Cl_2 \cdot [Et_3PH]Cl$ (**1a**), $[Au_2(tfepm)_3]Cl_2$ (**1b**), and $[Au(dppm)_2Rh(CN^tBu)_2]Cl_2$ (**2**).

	1a	**1b**	**2**
Empirical formula	$C_{33.50}H_{47}Au_2Cl_4F_{36}O_{12}P_7$	$C_{39}H_{54}Au_2Cl_2F_{36}O_{15}P_6$	$C_{63}H_{68}AuCl_8N_2P_4Rh$
fw	2078.23	2097.48	1560.55
Temp (K)	100(2)	100(2)	150(2)
λ(Å)	0.71073	0.71073	0.71073
Space group	$P\bar{1}$	$P2_1/n$	$P2_1/c$
a(Å)	16.359(6)	17.378(6)	26.651(4)
b(Å)	20.111(7)	15.932(5)	13.2594(18)
c(Å)	23.920(9)	15.932(5)	18.991(3)
α(°)	75.856(8)	90	90
β(°)	71.150(7)	108.438(6)	102.282(3)
γ(°)	72.629(7)	90	90
V(Å^3)	7012(4)	7064(4)	6557.5(16)
Z	4	4	4
d_{calcd}(Mg/m^3)	1.969	1.972	1.581
Abs coeff(mm^{-1})	4.634	4.509	2.950
$R1$ [a]	0.0372	0.0209	0.0683
$wR2$ [a]	0.0870	0.0534	0.1595

[a] $R1 = \Sigma||F_o| - |F_c||/\Sigma|F_o|$; $wR2 = [\Sigma w(F_o^2 - F_c^2)^2/\Sigma w(F_o^2)^2]^{1/2}$.

Table B1a. Crystallographic data for $[Au(dmpm)_2Rh(CN^tBu)_2]Cl_2$ (**3**) and $[Au(tfepma)_2Rh(CN^tBu)_2]Cl_2$ (**5**).

	3	**5**
Empirical formula	$C_{23}H_{52}AuCl_8N_2P_4Rh$	$C_{28}H_{40}AuCl_2F_{24}N_4O_8P_4Rh$
fw	1064.02	1511.30
Temp (K)	100(2)	100(2)
λ(Å)	0.71073	0.71073
Space group	$P2_1/c$	$P2_1/c$
a(Å)	19.195(3)	23.5084(17)
b(Å)	17.085(2)	10.8700(8)
c(Å)	12.7127(17)	22.7017(16)
α(°)	90	90
β(°)	90.046(3)	116.5690(10)
γ(°)	90	90
V(Å^3)	4169.0(10)	5188.5(6)
Z	4	4
d_{calcd}(Mg/m^3)	1.695	1.935
Abs coeff(mm^{-1})	4.595	3.501
$R1$ [a]	0.0762	0.0323
$wR2$ [a]	0.1688	0.0773

[a] $R1 = \Sigma||F_o| - |F_c||/\Sigma |F_o|$; $wR2 = [\Sigma w(F_o^2 - F_c^2)^2/\Sigma w(F_o^2)^2]^{1/2}$.

B.3 Selected Bond Lengths and Angles

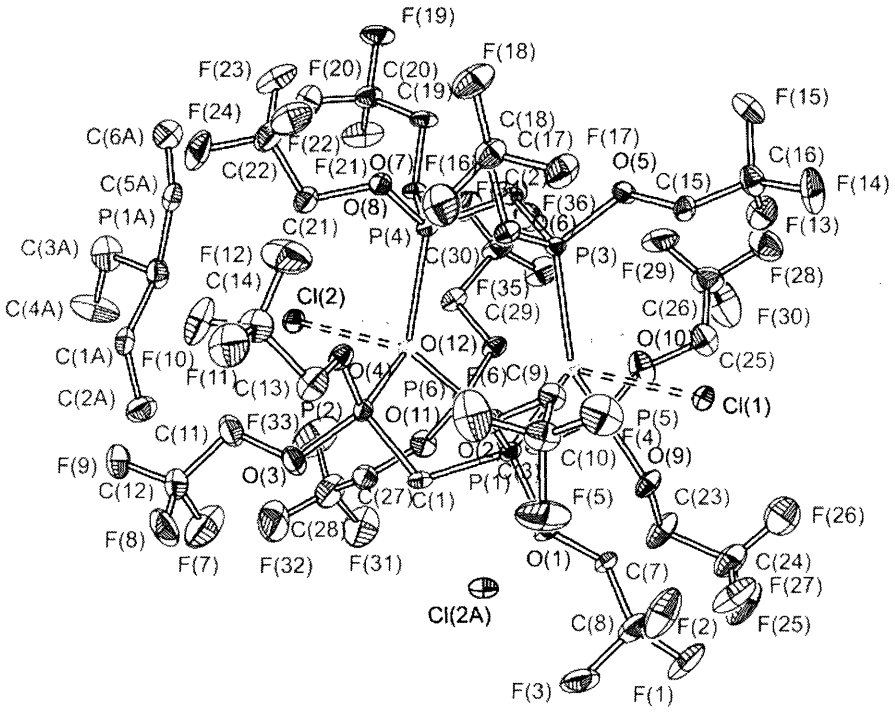

Table B2. Selected bond lengths (Å) and angles (°) of $[Au_2(tfepm)_3]Cl_2 \cdot [Et_3PH]Cl$ (**1a**).

Bond Lengths (Molecule 1)

Au(1)-P(5)	2.328(2)	Au(2)-P(2)	2.329(2)
Au(1)-P(3)	2.334(2)	Au(2)-P(6)	2.337(2)
Au(1)-P(1)	2.371(2)	Au(2)-P(4)	2.368(2)
Au(2)-Cl(2)	2.771(2)	Au(1)-Cl(1)	2.763(2)
P(1)-C(1)	1.804(8)	P(4)-C(2)	1.812(8)
P(2)-C(1)	1.812(8)	P(5)-C(3)	1.784(9)
P(3)-C(2)	1.814(8)	P(6)-C(3)	1.813(9)
Au(1)-Au(2)	3.5453(9)		

Bond Angles (Molecule 1)

P(5)-Au(1)-P(3)	126.09(8)	P(2)-Au(2)-P(6)	124.84(8)
P(5)-Au(1)-P(1)	114.28(8)	P(2)-Au(2)-P(4)	117.36(8)
P(3)-Au(1)-P(1)	115.98(8)	P(6)-Au(2)-P(4)	114.50(8)
P(5)-Au(1)-Cl(1)	95.25(8)	P(2)-Au(2)-Cl(2)	102.65(8)
P(3)-Au(1)-Cl(1)	102.40(7)	P(6)-Au(2)-Cl(2)	95.11(8)
P(1)-Au(1)-Cl(1)	90.63(8)	P(4)-Au(2)-Cl(2)	89.59(7)
P(1)-C(1)-P(2)	116.3(4)	P(4)-C(2)-P(3)	114.4(4)
P(5)-C(3)-P(6)	117.9(5)		

Bond Lengths (Molecule 2)

Au(3)-P(7)	2.332(2)	Au(4)-P(12)	2.327(3)
Au(3)-P(11)	2.345(2)	Au(4)-P(8)	2.349(2)
Au(3)-P(9)	2.394(2)	Au(4)-P(10)	2.375(2)
Au(3)-Cl(3)	2.852(2)	Au(4)-Cl(4)	2.793(2)
P(7)-C(4)	1.814(8)	P(10)-C(5)	1.820(9)
P(8)-C(4)	1.826(8)	P(11)-C(6)	1.810(8)
P(9)-C(5)	1.803(9)	P(12)-C(6)	1.799(9)
Au(3)-Au(4)	3.4718(11)		

Bond Angles (Molecule 2)

P(7)-Au(3)-P(11)	125.46(8)	P(12)-Au(4)-P(8)	123.50(9)
P(7)-Au(3)-P(9)	113.27(8)	P(12)-Au(4)-P(10)	118.71(9)
P(11)-Au(3)-P(9)	117.99(9)	P(8)-Au(4)-P(10)	115.42(8)
P(7)-Au(3)-Cl(3)	105.90(7)	P(12)-Au(4)-Cl(4)	100.27(8)
P(11)-Au(3)-Cl(3)	83.97(7)	P(8)-Au(4)-Cl(4)	96.81(8)
P(9)-Au(3)-Cl(3)	98.68(8)	P(10)-Au(4)-Cl(4)	87.65(8)
P(7)-C(4)-P(8)	113.2(4)	P(9)-C(5)-P(10)	114.2(5)
P(12)-C(6)-P(11)	115.6(4)		

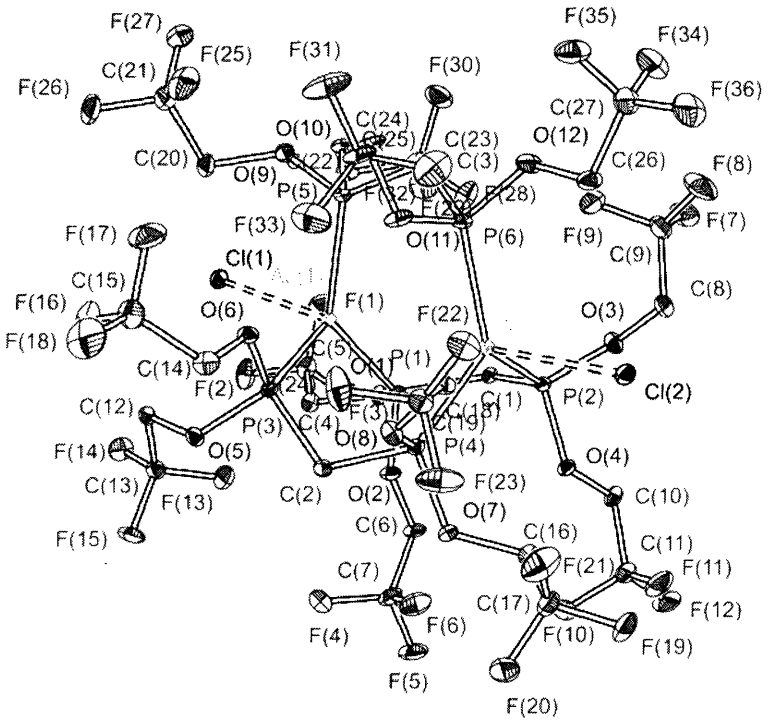

Table B3. Selected bond lengths (Å) and angles (°) of $[Au_2(tfepm)_3]Cl_2$ (**1b**).

	Bond Lengths		
Au(1)-Au(2)	3.5295(7)	Au(1)-Cl(1)	2.7713(10)
Au(1)-P(1)	2.3507(10)	Au(2)-P(2)	2.3514(10)
Au(1)-P(5)	2.3562(11)	Au(2)-P(6)	2.3665(11)
Au(1)-P(3)	2.3767(10)	Au(2)-P(4)	2.3918(11)
P(1)-C(1)	1.834(3)	P(4)-C(2)	1.815(4)
P(2)-C(1)	1.832(4)	P(5)-C(3)	1.828(4)
P(3)-C(2)	1.831(3)	P(6)-C(3)	1.828(4)
	Bond Angles		
P(1)-Au(1)-P(5)	127.50(4)	P(1)-Au(1)-Cl(1)	105.60(3)
P(1)-Au(1)-P(3)	111.35(3)	P(5)-Au(1)-Cl(1)	84.38(3)
P(5)-Au(1)-P(3)	116.26(3)	P(3)-Au(1)-Cl(1)	102.98(3)
P(2)-Au(2)-P(6)	124.61(3)	P(2)-C(1)-P(1)	113.79(18)
P(2)-Au(2)-P(4)	115.43(3)	P(4)-C(2)-P(3)	116.46(19)
P(6)-Au(2)-P(4)	117.49(3)	P(6)-C(3)-P(5)	115.16(19)

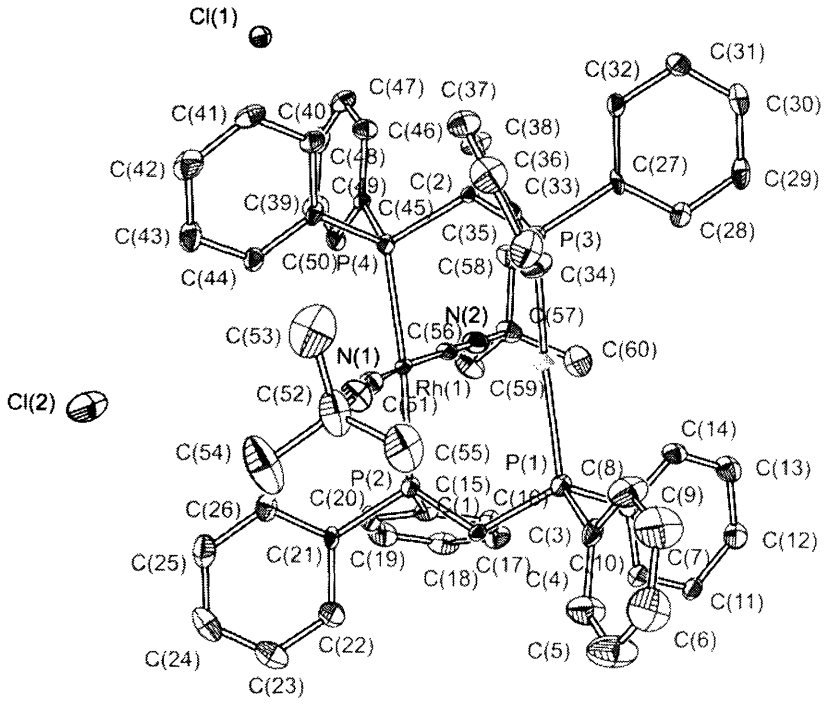

Table B4. Selected bond lengths (Å) and angles (°) of $[Au(dppm)_2Rh(CN^tBu)_2]Cl_2$ (**2**).

	Bond Lengths		
Au(1)-P(1)	2.314(3)	Au(1)-P(3)	2.316(3)
Rh(1)-P(2)	2.314(3)	Rh(1)-P(4)	2.323(3)
P(1)-C(1)	1.792(10)	P(3)-C(2)	1.819(9)
P(2)-C(1)	1.853(9)	P(4)-C(2)	1.844(10)
Au(1)-Rh(1)	2.9214(9)		
	Bond Angles		
P(1)-Au(1)-P(3)	173.01(10)	P(2)-Rh(1)-P(4)	174.99(10)
C(56)-Rh(1)-P(4)	90.0(3)	C(56)-Rh(1)-P(2)	90.7(3)
C(51)-Rh(1)-P(4)	91.2(3)	C(51)-Rh(1)-P(2)	88.9(3)
P(3)-C(2)-P(4)	117.4(5)	P(1)-C(1)-P(2)	119.4(5)
C(56)-Rh(1)-C(51)	171.6(4)		

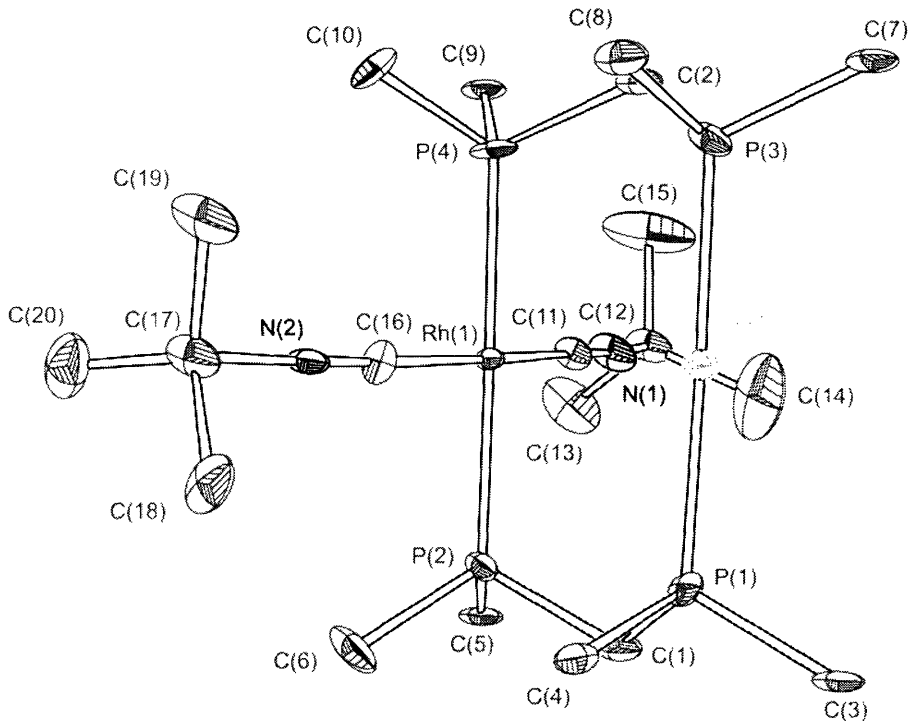

Table B5. Selected bond lengths (Å) and angles (°) of $[Au(dmpm)_2Rh(CN^tBu)_2]Cl_2$ (**3**).

	Bond Lengths		
Au(1)-P(1)	2.311(4)	Rh(1)-P(4)	2.310(4)
Au(1)-P(3)	2.311(4)	Rh(1)-P(2)	2.313(4)
P(1)-C(1)	1.830(16)	P(3)-C(2)	1.816(17)
P(2)-C(1)	1.834(17)	P(4)-C(2)	1.812(17)
Au(1)-Rh(1)	2.9666(14)		
	Bond Angles		
P(1)-Au(1)-P(3)	174.17(15)	P(4)-Rh(1)-P(2)	176.89(17)
C(16)-Rh(1)-P(2)	90.7(5)	C(16)-Rh(1)-P(4)	91.1(5)
C(11)-Rh(1)-P(2)	89.8(5)	C(11)-Rh(1)-P(4)	88.1(5)
P(1)-C(1)-P(2)	114.3(8)	P(4)-C(2)-P(3)	115.7(8)
C(16)-Rh(1)-C(11)	173.7(6)		

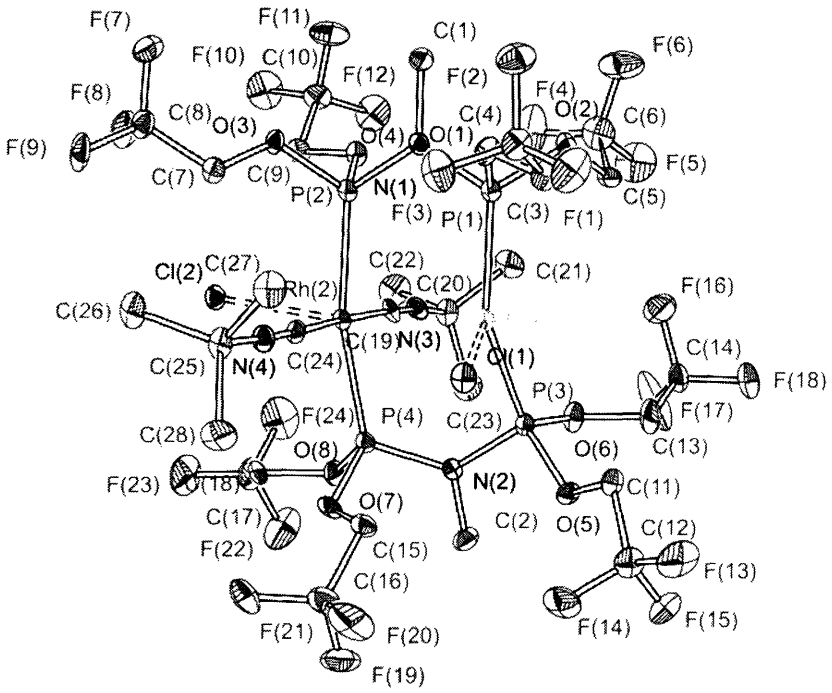

Table B6. Selected bond lengths (Å) and angles (°) of $[Au(tfepma)_2Rh(CN^tBu)_2]Cl_2$ (**5**).

Bond Lengths

Au(1)-P(3)	2.2664(14)	Au(1)-P(1)	2.2663(14)
Rh(2)-P(4)	2.2564(14)	Rh(2)-P(2)	2.3109(14)
Au(1)-Cl(1)	2.6564(13)	Rh(2)-Cl(2)	2.6034(13)
Rh(2)-C(19)	1.952(6)	Rh(2)-C(24)	1.980(6)
P(1)-N(1)	1.673(4)	P(3)-N(2)	1.680(4)
P(2)-N(1)	1.673(4)	P(4)-N(2)	1.681(4)
Au(1)-Rh(2)	2.8186(5)		

Bond Angles

P(3)-Au(1)-P(1)	151.36(5)	P(4)-Rh(2)-P(2)	166.48(5)
P(3)-Au(1)-Cl(1)	101.14(5)	P(1)-Au(1)-Cl(1)	101.35(4)
C(19)-Rh(2)-P(4)	83.93(16)	C(19)-Rh(2)-P(2)	87.09(16)
C(24)-Rh(2)-P(4)	94.30(15)	C(24)-Rh(2)-P(2)	93.84(15)
P(3)-N(2)-P(4)	120.3(3)	P(2)-N(1)-P(1)	121.5(3)
C(19)-Rh(2)-C(24)	175.2(2)		

C Appendix 3—Computational Details

C.1 Computational Methods

Calculations were performed using the Gaussian 98 program suite.[1] DFT calculations were carried out using the exchange functional of Becke[2] in conjunction with the P86 correlation functional of Perdew.[3] Los Alamos effective core potentials were applied to Rh and Au with the standard double zeta basis set of Hay and Wadt (LANL2DZ),[4-6] for all other atoms the 6-31G** basis set of Pople and coworkers was employed.[7,8] Geometry optimizations proceeded without symmetry restrictions and were initiated from coordinates obtained from crystallographically characterized complexes. Optimized geometries were confirmed as energy minima by frequency calculations. Flourine was substituted for the $-OCH_2CF_3$ groups on the tfepma ligands and $-CH_3$ for ^{t}Bu on *tert*-butylisonitrile to reduce computational intensity. Loosely associated chloride anions were removed prior to calculation. Singlet and triplet electronic excitations were investigated using time dependent DFT methods. All calculations are performed in the gas phase and no attempt has been made to account for the effects of solvation. Orbitals were imaged using the program Molekel,[9,10] default isodensity values were applied.

C.2 Structural Comparison between Experimental and Calculated Complexes

Table C1. Selected Bond lengths (Å) and angles (°) comparison for $[Au(dmpm)_2Rh(CN^tBu)_2]Cl_2$ (**4**) and $[Au(dmpm)_2Rh(CNMe)_2]^{2+}$ (**4a**).

Bond Lengths

	Exper.	Calculated		Exper.	Calculated
Au(1)-P(1)	2.311(4)	2.373	Rh(1)-P(4)	2.310(4)	2.358
Au(1)-P(3)	2.311(4)	2.374	Rh(1)-P(2)	2.313(4)	2.358
P(1)-C(1)	1.830(16)	1.862	P(3)-C(2)	1.816(17)	1.862
P(2)-C(1)	1.834(17)	1.874	P(4)-C(2)	1.812(17)	1.874
Rh(1)-C(11)	1.970(16)	1.967	Rh(1)-C(16)	1.968(16)	1.967
Au(1)-Rh(1)	2.9666(14)	3.021			
		Av. Deviation	.041		

Bond Angles

	Exper.	Calculated
P(1)-Au(1)-P(3)	174.17(15)	172.7
C(16)-Rh(1)-P(2)	90.7(5)	88.9
C(11)-Rh(1)-P(2)	89.8(5)	91.1
P(1)-C(1)-P(2)	114.3(8)	116.2
C(16)-Rh(1)-C(11)	173.7(6)	169.3
P(4)-Rh(1)-P(2)	176.89(17)	179.1
C(16)-Rh(1)-P(4)	91.1(5)	91.2
C(11)-Rh(1)-P(4)	88.1(5)	89.0
P(4)-C(2)-P(3)	115.7(8)	116.3
P(1)-Au(1)-Rh(1)-P(2)	–5.42 (15)	–8.5
P(3)-Au(1)-Rh(1)-P(4)	–1.35(16)	–8.4
Av. Deviation	2.3	

Table C2. Selected Bond lengths (Å) and angles (°) comparison for $[Au(tfepma)_2Rh(CN^tBu)_2]Cl_2$ (**5**) and $[Au(MeN(PF_2)_2)_2Rh(CNMe)_2]^{2+}$ (**5a**).

Bond Lengths

	Exper.	Calculated		Exper.	Calculated
Au(1)-P(3)	2.2664(14)	2.352	Au(1)-P(1)	2.2663(14)	2.353
Rh(2)-P(4)	2.2564(14)	2.290	Rh(2)-P(2)	2.3109(14)	2.290
Rh(2)-C(19)	1.952(6)	1.993	Rh(2)-C(24)	1.980(6)	1.993
P(1)-N(1)	1.673(4)	1.685	P(3)-N(2)	1.680(4)	1.685
P(2)-N(1)	1.673(4)	1.715	P(4)-N(2)	1.681(4)	1.715
Au(1)-Rh(2)	2.8186(5)	2.881	Au(1)-P(1)	2.2663(14)	2.353
		Av. Deviation	.045		

Bond Angles

	Exper.	Calculated
P(3)-Au(1)-P(1)	151.36(5)	174.5
C(19)-Rh(2)-P(4)	83.93(16)	90.0
C(24)-Rh(2)-P(4)	94.30(15)	90.0
P(3)-N(2)-P(4)	120.3(3)	122.2
C(19)-Rh(2)-C(24)	175.2(2)	170.2
P(4)-Rh(2)-P(2)	166.48(5)	179.1
C(19)-Rh(2)-P(2)	87.09(16)	90.1
C(24)-Rh(2)-P(2)	93.84(15)	90.0
P(2)-N(1)-P(1)	121.5(3)	122.2
P(1)-Au(1)-Rh(2)-P(2)	6.06(5)	0.1
P(3)-Au(1)-Rh(2)-P(4)	23.60(5)	0.2
Av. Deviation	8.2	

C.3 TD-DFT Calculated Singlet Transition Energies

Table C3. TD-DFT calculated singlet transition energies for complexes **4a**, and **5a**.

Complex	Transition	f[a]	λ_{calc} (nm)	λ_{obs} (nm)
	HOMO → LUMO	0.1060	482	448
4a	HOMO → LUMO +1	0.0036	385	
	HOMO –1 → LUMO	0.0215	376	331
	HOMO → LUMO	0.1329	456	
5a	HOMO → LUMO +1	0.0056	389	355
	HOMO –1 → LUMO	0.0490	375	297

[a] Oscillator strength

References

(1) Frisch, M. J.; Trucks, G. W.; Schlegel, H. B.; Scuseria, G. E.; Robb, M. A.; Cheeseman, J. R.; Zakrzewski, V. G.; Montgomery, J. A., Jr.; Stratmann, R. E.; Burant, J. C.; Dapprich, S.; Millam, J. M.; Daniels, A. D.; Kudin, K. N.; Strain, M. C.; Farkas, O.; Tomasi, J.; Barone, V.; Cossi, M.; Cammi, R.; Mennucci, B.; Pomelli, C.; Adamo, C.; Clifford, S.; Ochterski, J.; Petersson, G. A.; Ayala, P. Y.; Cui, Q.; Morokuma, K.; Malick, D. K.; Rabuck, A. D.; Raghavachari, K.; Foresman, J. B.; Cioslowski, J.; Ortiz, J. V.; Stefanov, B. B.; Liu, G.; Liashenko, A.; Piskorz, P.; Komaromi, I.; Gomperts, R.; Martin, R. L.; Fox, D. J.; Keith, T.; Al-Laham, M. A.; Peng, C. Y.; Nanayakkara, A.; Gonzalez, C.; Challacombe, M.; Gill, P. M. W.; Johnson, B. G.; Chen, W.; Wong, M. W.; Andres, J. L.; Head-Gordon, M.; Replogle, E. S.; Pople, J. A. *Gaussian 98*, revision A.9; Gaussian, Inc.: Pittsburgh, PA, 1998.

(2) Becke, A. D. *Phys. Rev. A* **1988**, *38*, 3098- 3100.

(3) Perdew, J. P. *Phys. Rev. B* **1986**, *33*, 8822-8824.

(4) Hay, P. J.; Wadt, W. R. *J. Chem. Phys.* **1985**, *82*, 270-283.

(5) Wadt, W. R.; Hay, P. J. *J. Chem. Phys.* **1985**, *82*, 284-298.

(6) Hay, P. J.; Wadt, W. R. *J. Chem. Phys.* **1985**, *82*, 298-310.

(7) Hariharan, P. C.; Pople, J. A. *Theor. Chim. Acta* **1973**, *28*, 213-222.

(8) Francl, M. M.; Pietro, W. J.; Hehre, W. J.; Binkley, J. S.; Gordon, M. S.; DeFrees, D. J.; Pople, J. A. *J. Chem. Phys.* **1982**, *77*, 3654-3655.

(9) Flükiger, P.; Lüthi, H. P.; Portmann, S.; Weber, J. *MOLEKEL 4.3*; Swiss Center for Scientific Computing: Manno, Switzerland, 2000-2002.

(10) Portmann, S.; Lüthi, H. P. MOLEKEL: An Interactive Molecular Graphics Tool. *Chimia* **2000**, *54*, 766-770.

D Acknowledgements

First and foremost, I would like to thank my research advisor and mentor, Daniel Nocera, for giving me the chance to work on this exciting project. Your attention, guidance, and patience have been truly more than I could have wished for. Thank you for allowing me to explore the facets of this project I found most intriguing. Thank you also for being so kind and approachable, and for taking time to see that I gained as much as possible from my research experience. I will never forget all that I learned from you.

Next, I would like to thank the wonderful members of the Nocera Group. Your never-ending patience has been extraordinary, and I have learned so much from working alongside all of you. David Manke, I could not have done this without you. You have always been there to answer my "kestions" and to make me laugh. You've taught me my experimental technique, how to solve a crystal structure, and most importantly, how to approach questions in chemistry. Thank you for your dedication, attention, and patience—and for supporting my taste in country music. Steven Reece, I cannot thank you enough for introducing me to the world of lasers and spectroscopy. Your interest in my project and my education as a chemist has been extraordinary, and this project would not have gone as far as it has without you. Your ideas, thoughts, and explanations have always been insightful and helped me better understand the things I have pursued. Your patience during the long hours spent in the basement will not be forgotten. Arthur Esswein, thank you for being my "box buddy." You've always been there to answer my dumb questions, and probed me to think more about my experiments. Thank you for not yelling at me when I dropped your vial of tfepm and for teaching me how to use the high vacuum line. Julien Bachmann, thank for always being so cheerful and helpful, day in and day out. You've always given attention to my questions, and I appreciate your genuine support, patience and help. Thank you also for teaching me E-chem and how to perform ADF calculations so that I could do such a great job with my 5.05 project. Aetna Wun, thank you for spending grueling hours trying to help me use the cryostat and the fluorometer concurrently. Also, thank you for always making sure I was involved in group events and making me feel included. Your kindness is more than anyone could ask for, and I wish you the best of luck next year. Adam Veige, thank you for mentoring me as I embarked on the Au-Rh project. You taught me a great deal about researching a project from the ground up, and helped me become more aggressive with my experiments. Elizabeth

Young, thank you for teaching me how to use the fluorometer, for helping me collect data with the picosecond laser, and for improving my squash game. Bart Bartlett, thank you for being the best desk neighbor I could ask for, and always making me smile. Thank you to Joel Rosenthal for being a great ex-desk neighbor, always giving me a reason to procrastinate around my bench, and for giving my beautiful necklaces. Thank you to Jake Soper and Matt Shores for being coolest pre-professors ever. Remember, you promised me a post-doc. Thank you to Glen Alliger, Deqiang An, Thomas Gray, Justin Hodgkiss, Shih-yuan Liu, T.D. Luckett, Gretchen Kappelmann, Alex Krivokapic, Kate Markiewicz, Emily Nytko, Preston Snee, and Jenny Yang for your kindness and all the good times we've had together. Lastly, I'd like to thank Becky Somers, for her support, encouragement and wonderful friendship.

Next, I'd like to thank the MIT Department of Chemistry. I do not imagine I could have learned the platforms and tenets of this great science is such a rigorous and deep manner from any other school. I would like to thank, in particular, Professor Andre Tokamakoff and Professor Joseph Sadighi for their kindness, encouragement, and guidance. I would also like to thank the Undergraduate Research Opportunities Program for financial support.

I'd like to thank my friends who have helped make my experience at MIT simply incredible. My best friend, Stavroula Hatzios, who underwent the UROP experience alongside me, has always been there when it was time get out of lab and have fun. Sarah Buckley, Dale Cotton, Karen Keller, Sam Schweighart, Rachel Williams, Nick Wyhs and all the other members of MIT EMS have always made me smile, on and off the ambulance.

I'd like to thank my family—Thomas, Rochelle, Elizabeth and Scott Dempsey, for their continued love, encouragement, and support.

Lastly, I'd like to thank Neal Mankad, who shares my passion for chemistry and continues to inspire and support my dedication to the science. I thank you for all our thought provoking discussions which have given me great insight into the nature of molecules, for emotionally supporting me through the turmoil of lab, and most of all, for your love.